A&A, 708, A244 (2026)
https://doi.org/10.1051/0004-6361/202557624
© The Authors 2026

Astronomy & Astrophysics

# The baryon budget of galaxies across the first billion years

## Theoretical predictions for gas phases, depletion times, stellar return fractions

Umberto Maio[1,2,★] and Céline Péroux[3,4]

[1] INAF-Italian National Institute of Astrophysics, Observatory of Trieste, Via G. Tiepolo 11, 34143 Trieste, Italy
[2] Institute for Fundamental Physics of the Universe, Via Beirut 2, 34151 Trieste, Italy
[3] European Southern Observatory, Karl-Schwarzschild-Straße 2, 85748 Garching bei Muenchen, Germania
[4] Aix Marseille Université, CNRS, LAM (Laboratoire d'Astrophysique de Marseille) UMR 7326, 13388 Marseille, France

Received 9 October 2025 / Accepted 15 February 2026

**ABSTRACT**

*Context.* ALMA and JWST observations of galaxies in the first billion years of the Universe provide key constraints on the baryon cycle during the epoch of reionisation. A complete census of the baryonic phases in early galaxies is essential to understand the efficiency and timescales of star formation.
*Aims.* In this work, we study cosmic matter at redshift $z > 5$ to investigate the different phases in which early gas and stars reside, their corresponding mass budgets, the resulting depletion times, and the expected stellar return fraction as a function of stellar age.
*Methods.* We used the ColdSIM hydrodynamical time-dependent non-equilibrium chemistry simulations to perform a detailed analysis of the cold, warm, hot, and stellar phases for both bound structures (galaxies and their circumgalactic medium) and the diffuse intergalactic medium. We further investigated the cold HI and $H_2$ components, explicitly computed in our simulations, and examined their relations with the host mass, star formation, metallicity, and depletion timescales. We also provide observational insights and discuss the implications for stellar mass functions, Population III star formation, and changes in the initial mass function.
*Results.* Cosmic gas prior to reionisation is mostly cold, while at later epochs the warm phase becomes dominant as a consequence of enhanced star formation activity and increasing UV reionising radiation. Stellar return fractions at these times are ~0.15–0.20, a factor of two lower than the values usually adopted. Mass functions and mass density parameters in bound objects increase with cosmic time, closely tracing the overall structure formation process. Cold, warm, and hot gas masses as well as HI and $H_2$ components show increasing trends with mass and star formation rate, while HI and $H_2$ depletion times decrease down to 0.01–0.1 Gyr with a weak dependence on metallicity. The resulting star formation efficiency remains at the level of a few percent independently of $z$ and gas-to-star fractions decline with mass, influenced by local feedback and environment. Our findings are consistent with ALMA, VLA and IRAM surveys at later epochs, including ALFALFA, xCOLDGASS, GASS, xGASS, EDGE-CALIFA, PHIBBS, and ASPECS.
*Conclusions.* Gas phases are quantitatively related to the underlying stellar populations and can be used to infer unknown quantities. In the appendix, we provide fit functions describing the trends of the stellar return fraction, the main sequence, phase mass relations, gas-to-star fractions, and depletion timescales.

**Key words.** galaxies: formation – galaxies: high-redshift – intergalactic medium – galaxies: star formation

## 1. Introduction

Baryonic structure formation relies on a scenario in which cosmic gas falls into the galaxy potential wells from large scales, cools down, and condenses into stars. Formed stars release energy and mass into the surrounding medium via star formation feedback that, together with active galactic nucleus (AGN) activity, leads baryon outflows. This determines a continuous mass transfer among different baryon phases and scales, during which matter flows in and out of galaxies: the so-called baryon cycle (e.g. Tumlinson et al. 2017; Péroux & Howk 2020). This latter essentially mediates the interplay between cosmic mass that is gravitationally bound in galaxies and the intergalactic medium (IGM). Primordial times witness the very first episodes of the cosmic baryon cycle, which is likely in place by the first half-gigayear of the Universe.

Recent JWST and ALMA detections (Bañados et al. 2024; Chemerynska et al. 2024; Carniani et al. 2024; Huertas-Company et al. 2025; Schouws et al. 2025a,b; Helton et al. 2025a; Naidu et al. 2026; Conselice et al. 2025; Fujimoto et al. 2025; Gandolfi et al. 2025) suggest that the first galaxies have already formed by redshift $z \simeq 14$ and present relatively complex metallicity ($Z$) patterns with a star-forming main sequence established over timescales of 10–100 Myr. The onset of such early star formation episodes requires significant amounts of cold molecular ($H_2$) mass. Indeed, neutral hydrogen (HI) and helium are not efficient coolants below about $10^4$ K, but HI and residual free electrons trigger the formation of large quantities of $H_2$ both in pristine population III (PopIII) and in polluted population II-I (PopII-I) regimes (Saslaw & Zipoy 1967; Hollenbach & McKee 1979; Abel et al. 1997; Galli & Palla 1998; Maio et al. 2010; Wise et al. 2012; Huyan et al. 2025; Vanzella et al. 2026).

Cold or cooling gas is commonly observed in galaxies through HI 21 cm line or molecular transitions. Warm gas is usually seen in star-forming sites via photoionisation emission in $H_\alpha$ or high-ionisation metal species and expected in optically thick regions of MHD-driven accretion discs. With high-energy instruments, such as eRosita or XRISM, hot (2–10 keV)

★ Corresponding author: umberto.maio@inaf.it



Open Access article, published by EDP Sciences, under the terms of the Creative Commons Attribution License (https://creativecommons.org/licenses/by/4.0), which permits unrestricted use, distribution, and reproduction in any medium, provided the original work is properly cited.
This article is published in open access under the Subscribe to Open model. Subscribe to A&A to support open access publication.

gas can be found in optically selected objects at $z \simeq 0$–2, X-ray emitting galaxy clusters, and AGN coronas (Jiang et al. 2019; Comparat et al. 2023). Resolved active-galaxy studies in the local Universe have detected kiloparsec-scale molecular outflows with strong contributions from the $H_2$ phase at temperatures of $T \gtrsim 10^3$ K (Cicone et al. 2014, 2021; Lamperti et al. 2022; Zanchettin et al. 2025; Koribalski et al. 2025; Langan et al. 2026), while MUSE observations indicate the presence of $\sim 10^2$ K molecular gas in galaxies that are both accreting and expelling material (Weng et al. 2022). Despite the evidence that baryons can be found in a broad variety of phases and objects, quantitative estimates are challenging.

The relations between cold neutral gas (detected in absorption) and warm ionised gas (probed in emission) are currently being explored. Recent comparative studies involving controlled samples at $z \simeq 2$–4 have found a typical variance in the probed gas abundances of 0.2-0.3 dex with dependencies on the line diagnostic used (Schady et al. 2024). This approach opens the possibility of combining both absorption and emission techniques to better investigate high-$z$ faint galaxies (Kulkarni et al. 2022). Nevertheless, theoretical studies focusing on high-$z$ gas phases are still lacking and the contribution of cold, warm, and hot gas to the whole cosmic mass budget is to be determined.

It is known from both observational results and theoretical calculations that at $z < 6$, after reionisation completes, the cosmic mass density of cold neutral gas flattens around $10^{-3}$ of the cosmic critical density (Wolfe et al. 1995; Rao & Turnshek 2000; Storrie-Lombardi & Wolfe 2000; Péroux et al. 2001; Nagamine et al. 2004; Tacconi et al. 2020; Heintz et al. 2022). The condensed baryon budget is dominated by the HI component, while corresponding $H_2$ values are estimated to be much lower (between a factor of a few and some dex; Walter et al. 2020; Decarli et al. 2020; Maio et al. 2022; Boogaard et al. 2023; Messias et al. 2024). Previous studies have shown that warm or hot gas can account for a large fraction of baryons in low-redshift structures (e.g. Dev et al. 2024; Deepak et al. 2025), but at high $z$ the situation is extremely uncertain and their share, distribution, and evolution is debated (Peroux & Nelson 2024).

The interplay among different gas phases, the conversion of cold gas into stars and the release of stellar mass into warm and hot gas depend on a few physical quantities, i.e. gas depletion times ($t_{\rm depl}$), stellar ages ($t_{\rm age}$), and the stellar return fraction ($R$). A clear assessment of these variables is crucial for our understanding of the early baryon cycle, as well as for addressing the connection between gas and stars. Low-$z$ and cosmic-noon studies have suggested that typical depletion times might be of the order of some gigayears (Tacconi et al. 2013, 2018; Castignani et al. 2025; Kaur et al. 2025), while commonly adopted values for $R$ are obtained by averaging over a chosen initial stellar mass function (IMF) and imposing instantaneous recycling of massive stars (Maeder 1992; Madau & Dickinson 2014). That means that stellar ages and time-dependent yields are not taken into account. Thus, resulting $R$ values, typically in the range of $R \simeq 0.3$–$0.4$ for Salpeter (1955) and Kroupa (2001) or Chabrier (2003) IMFs, can be considered valid only on timescales of 5–10 Gyr. Due to the much shorter cosmic times at $z \gtrsim 5$, those findings are unreliable for such an epoch. Hence, depletion times and stellar return fractions should be revised and reconciled with high-$z$ timescales. This is relevant for estimating stellar masses and star formation rates (SFRs) in the early Universe.

Throughout this work, we shed light on these issues by using ad hoc hydrodynamical simulations of primordial structure formation taken by the ColdSIM project (e.g. Maio et al. 2022; Casavecchia et al. 2024; Parente et al. 2026). We adopt a $\Lambda$ cold dark matter ($\Lambda$CDM) model with present-day cosmological-constant, matter, and baryon density parameters of $\Omega_{0,\Lambda} = 0.726$, $\Omega_{0,\rm m} = 0.274$, and $\Omega_{0,\rm b} = 0.0458$, respectively. The expansion parameter normalised to 100 km/s/Mpc is $h = 0.702$, while the mass variance within 8 Mpc/$h$ radius is $\sigma_8 = 0.816$ and the power spectrum index is $n = 0.968$ (Planck Collaboration VI 2020). The comoving cosmological critical density is $\rho_{0,\rm crit} = 277.4\,h^2 {\rm M}_\odot\,{\rm kpc}^{-3} = 136.7\,{\rm M}_\odot\,{\rm kpc}^{-3}$ and the value of the metallicity in the solar neighbourhood is $Z_\odot = 0.02$. All logarithms are in base 10.

The text is organised as follows. In Sect. 2, we describe the numerical simulations used and the analysis performed. In Sect. 3 we show our main results and in Sect. 4 we discuss them. We then summarise our findings and conclude in Sect. 5. Fitting relations and supplementary material are collected in the appendix.

## 2. Method

We employed the detailed and accurate ColdSIM numerical simulations of primordial cosmic structure formation. The implementation includes gravitational-force calculations and smoothed-particle hydrodynamics inherited from the P-Gadget-3 code (Springel 2005) and additional extensions including: non-equilibrium atomic and molecular chemistry (for $e^-$, H, $H^+$, $H^-$, He, $He^+$, $He^{++}$, $H_2$, $H_2^+$, D, D+, HD, and $HeH^+$) explicitly followed in cold, warm, and hot gas phases; dust grain catalysis; photoelectric and cosmic-ray heating; HI and $H_2$ density-dependent self-shielding; gas cooling from resonant and sub-millimetre fine-structure line emission; star formation and stellar evolution of PopII-I and PopIII stars according to a Salpeter IMF; remnant masses and metal spreading for He, C, N, O, Ne, Mg, Si, S, Ca, and Fe, from type-II and type-Ia supernovae (SNe) and asymptotic-giant-branch (AGB) events according to metal-dependent yields and lifetimes; thermal feedback; and galactic winds (kinetic feedback) at 350 km/s (Maio et al. 2022; Maio & Viel 2023; Casavecchia et al. 2024, 2025; Parente et al. 2026). PopIII and PopII-I regimes are differentiated in terms of a critical metallicity $Z_{\rm crit} = 10^{-4}\,Z_\odot$ and differ for the stellar metal yields adopted. Yields for zero-metallicity stars are used in the PopIII case ($Z < Z_{\rm crit}$) and yields for metal-enriched stars in the PopII-I case ($Z \geq Z_{\rm crit}$). We remind the reader that $Z_{\rm crit}$ values are quite uncertain (Bromm et al. 2001a; Omukai et al. 2005; Santoro & Shull 2006; Chiaki et al. 2014; Chon et al. 2024), but, due to the rapid metal enrichment by early SNe, different assumptions do not lead to significantly different results (Maio et al. 2010).

We consider three cosmic volumes initialised at redshift $z = 99$ according to the $\Lambda$CDM paradigm. Our reference (Ref) set-up has a comoving box side of $L = 10\,{\rm Mpc}/h$ and an initial number of gas and dark-matter particles of $N_{\rm part} = 2 \times 512^3$. The high-resolution (HR) run has the same $L$, and $N_{\rm part} = 2 \times 1000^3$, while the large-box (LB) run is characterised by $L = 50\,{\rm Mpc}/h$ and $N_{\rm part} = 2 \times 1000^3$. We performed our analysis on the Ref run and checked the effects of resolution or volume sampling by comparisons with the HR and LB simulations in Appendix A and B. The resulting gas ($m_{\rm gas}$) and dark-matter ($m_{\rm dm}$) mass resolutions are listed in Table 1.

Cosmic structures were identified by searching for clustered particles via a friend-of-friend technique with a linking length of $\sim$0.2 the mean inter-particle separation. A substructure finder

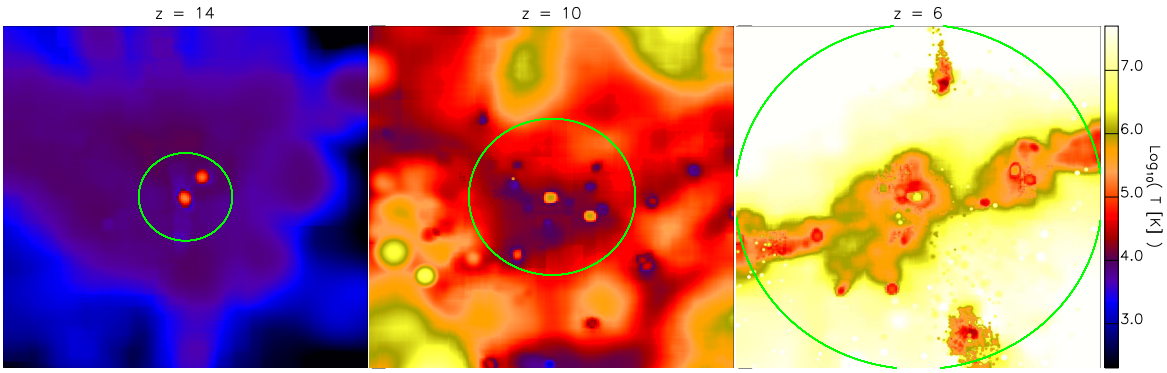



**Fig. 1.** Mass-weighted temperature maps at $z \simeq 14$, 10 and 6 smoothed on a grid of 1024 pixels a side for the gas in the largest halo that has a physical virial radius (circles) of ~2.4, 5.9, and 18.7 kpc and a total mass of $1.4 \times 10^9$, $7.3 \times 10^9$, and $6.9 \times 10^{10}$ $M_\odot$, respectively, from left to right.

**Table 1.** Simulation set-up for the HR, Ref, and LB runs.

| Name | $L$[Mpc] | $N_{\rm part}$ | $m_{\rm gas}[M_\odot/h]$ | $m_{\rm dm}[M_\odot/h]$ |
|---|---|---|---|---|
| HR | 14 | $2 \times 1000^3$ | $1.27 \times 10^4$ | $6.34 \times 10^4$ |
| Ref | 14 | $2 \times 512^3$ | $9.47 \times 10^4$ | $4.72 \times 10^5$ |
| LB | 71 | $2 \times 1000^3$ | $1.58 \times 10^6$ | $7.93 \times 10^6$ |

**Table 2.** Gas phase definitions.

| Gas phase | cold | warm | hot |
|---|---|---|---|
| Temperature | $T < 10^4$ K | $10^4 \leq T/\mathrm{K} \leq 10^7$ | $T > 10^7$ K |

algorithm checked for minimal values of the local gravitational potential and gave us basic properties of gravitationally bound structures (Dolag et al. 2009), such as the position, virial radius ($R_{\rm vir}$), virial mass ($M_{\rm vir}$), stellar mass ($M_{\rm star}$), SFR, and $Z$. To avoid numerical artefacts that could have led to spurious results, we considered bound structures to be well behaved only if they were sampled with at least 300 particles and their $R_{\rm vir} > 0$. A pictorial view of such cosmic objects is given in Fig. 1, where the projected mass-weighted temperature is shown for the most massive halo at $z \simeq 6$ traced back to $z \simeq 10$ and 14 when its total mass is $6.9 \times 10^{10}$, $7.3 \times 10^9$, and $1.4 \times 10^9$ $M_\odot$, and its physical virial radius is 18.7, 5.9, and 2.4 kpc, respectively. For all the simulated objects, we additionally evaluated the masses in the cold, warm, and hot gas phase defined as the ones with gas temperatures of $T < 10^4$ K, $10^4 \leq T/\mathrm{K} \leq 10^7$, and $T > 10^7$ K (Table 2). From the abundances derived by our chemistry network, we explicitly computed the HI and $H_2$ masses, too. Our modelling produces a main sequence characterised by a rather flat specific-SFR (sSFR) trend with $M_{\rm star}$, in agreement with available observations (Appendix C). The simulated sequence at $z > 5$ can be fitted by

$$\mathrm{Log}(\mathrm{sSFR}/\mathrm{Gyr}^{-1}) = 1.871 - 0.187\,\mathrm{Log}(M_{\rm star}/M_\odot) \quad (1)$$

and analogous relations hold at different $z$ (Appendix C).

The resulting SFR density (SFRD) is in line with recent observational data, as shown in our previous works (e.g. Fig. 2 in Casavecchia et al. 2024), where resolution impacts for the Ref, LB, and HR runs are discussed, as well.

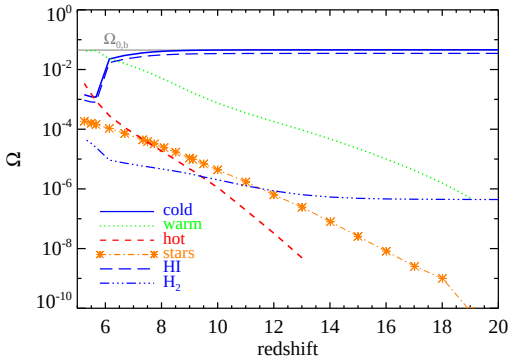



**Fig. 2.** Baryon density parameters as function of redshift for cold (solid line), warm (dotted line), hot (short-dashed line), stellar (dot-dashed line with asterisks), HI (long-dashed line), and $H_2$ (dot-dot-dot-dashed line) phases. The horizontal grey line marks the value of $\Omega_{0,b}$.

## 3. Results

In the next sections, we present our main results about the cosmic baryon census and the links among different mass phases. We first present global trends (Sect. 3.1), then we study the relations between baryon phases and galaxy properties (Sect. 3.2). Finally, we address the picture for the baryon cycle (Sect. 3.3).

### 3.1. Global trends

Mass density parameters and mass functions are shown below.

#### 3.1.1. Mass density parameters

Baryon mass density parameters in the simulated cosmic volume were computed as: $\Omega_{\rm phase} = \rho_{\rm phase}/\rho_{0,\rm crit}$, with $\rho_{\rm phase}$ comoving mass density of the given baryonic phase considered (cold, warm, hot, stars, HI, $H_2$).

Results for $\Omega_{\rm cold}$, $\Omega_{\rm warm}$, $\Omega_{\rm hot}$, $\Omega_{\rm stars}$, $\Omega_{\rm HI}$, and $\Omega_{\rm H_2}$ are shown in Fig. 2. From the trends it is clear that at $z \gtrsim 6$ the cold phase dominates the cosmic mass budget, with a mass density parameter that closely traces $\Omega_{0,b}$. At $z \lesssim 6$, reionisation gets completed and $\Omega_{\rm cold}$ drops by almost two orders of magnitudes, stabilising around $10^{-3}$ (possibly linked to surviving neutral islands; Malloy & Lidz 2015; Becker et al. 2015; Bosman et al. 2018; Kulkarni et al. 2019; Nasir & D'Aloisio 2020; Gnedin & Zhu 2025; Becker et al. 2024; Spina et al. 2024; Zhu et al. 2024; Davies et al. 2026), while the warm component catches up and

**Table 3.** Impact of IMF variation on stellar masses.

| IMF variation | Stellar-mass change (factor) |
|---|---|
| From Salpeter to Chabrier | Reduce by 0.243 dex (1.75) |
| From Chabrier to Kroupa | Reduce by 0.057 dex (1.14) |
| From Salpeter to Kroupa | Reduce by 0.3 dex (2.00) |
| From diet Salpeter to Salpeter | Increase by 0.15 dex (1.41) |
| From diet Salpeter to Chabrier | Reduce by 0.093 dex (1.24) |

becomes the most important mass reservoir at later times. At early epochs, $\Omega_{\rm warm}$ is driven by star formation feedback and its contribution is as low as $\sim 10^{-6}$ at $z \sim 20$, about 5 dex smaller than $\Omega_{\rm cold}$. Ongoing star formation heats up cold material and triggers the conversion of increasingly large amounts of cold gas into warm gas between $z \sim 20$ and 6. This is reflected by the behaviour of $\Omega_{\rm stars}$, which accounts for a fraction of a percent of the mass involved in star-forming events (as traced by the warm phase). We note that the stellar budget was derived from a Salpeter IMF and that possible IMF variations (Kroupa 2001; Chabrier 2003; Bell & de Jong 2001; Bell et al. 2003; Gallazzi et al. 2008; Herrmann et al. 2016; Blackwell et al. 2026) impact $\Omega_{\rm stars}$ by up to 0.3 dex (a factor of 2), as summarised in Table 3.

Hot gas mass generated during cosmic structure assembly is subdominant, since it traces larger and rarer objects. The cold phase hosts both HI and $H_2$, two crucial species for the conversion of gas into stars. While HI typically accounts for 3/4 the cold mass, $H_2$ molecules are almost ubiquitous. Their production gets enhanced during the early gas collapse at $z \sim 15$–20 and increases by roughly two orders of magnitudes by $z \sim 5$.

### 3.1.2. Mass functions

Fig. 3 shows mass functions for cold, warm, and hot gas at $z \simeq 5$–16. The mass function is defined as the number of objects with a given (phase) mass per unit volume and per unit logarithmic mass bin. In all three cases, the mass function evolves from narrow, poorly sampled distributions ($z \simeq 16$) to broader and richer ones ($z \simeq 5$) with higher normalisation values towards lower redshifts. That is a direct consequence of cosmic structure formation, which causes an increase over time of the number density of formed galaxies. The cold and warm phases peak at $M_{\rm cold} \sim M_{\rm warm} \sim 10^7\,{\rm M}_\odot$ and the hot phase at $M_{\rm hot} \sim 10^5\,{\rm M}_\odot$ at roughly any $z$. The high-mass end of the distributions show that the maximum values of cold, warm, and hot masses are very different, with $M_{\rm cold}$ reaching $\sim 10^9\,{\rm M}_\odot$, but $M_{\rm warm} \sim 10^{10}\,{\rm M}_\odot$ and $M_{\rm hot}$ only $\sim 10^8\,{\rm M}_\odot$. Larger objects are able to retain larger amounts of baryons, while smaller objects have shallower potential wells, and hence are more susceptible to feedback energetics. A clear example is offered by the cold-phase mass distribution between $z \simeq 6$ and 5, when reionisation heats up cold, diffuse gas and leads to a decrease in the peak mass and the low-mass tail. At $z \gtrsim 6$ the redshift evolution is quite neat and regular and results from the interplay between local gas cooling and stellar heating. By comparing the masses of different gas phases at any fixed $z$, we find in general a minor role played by hot gas and a more relevant role played by cold and warm gas at most scales.

Looking at the details of cold-mass distributions, in Fig. 4 we make predictions for the HI and $H_2$ mass functions. The former closely follows the $M_{\rm cold}$ behaviour, as expected from its typical abundances (see Fig. 2); hence, the HI mass function is a reliable tracer of the cold-gas mass function. In the upper panel, we also show a fit derived by ALFALFA data and valid at $z = 0$ for $M_{\rm HI} > 10^6\,{\rm M}_\odot$ (Jones et al. 2018). Clearly, the low-redshift trend is not a good description of the high-$z$ HI distribution, when mass regimes and gas thermal states are rather different. In fact, the lack of early, grown, massive structures biases the resulting high-$z$ HI distributions towards values of $M_{\rm HI} < 10^9\,{\rm M}_\odot$. Halo mass growth and/or mergers at later times are expected to shift HI masses up to $M_{\rm HI} \simeq 10^{10}$–$10^{11}\,{\rm M}_\odot$ and reionisation would lower the abundance of smaller (mostly unshielded) objects with $M_{\rm HI} \sim 10^6$–$10^8\,{\rm M}_\odot$. The behaviour of the $H_2$ mass function is more convolved, because $M_{\rm H_2}$ can grow in a variety of temperature and density regimes and both stellar feedback and reionisation are efficient at dissociating unshielded $H_2$ mass. In particular, the high-$M_{\rm H_2}$ end is driven by molecular formation in thick cooling gas, while the low-mass tail is determined by $H_2$ destruction due to stellar feedback ($z > 6$) or reionisation ($z \lesssim 6$).

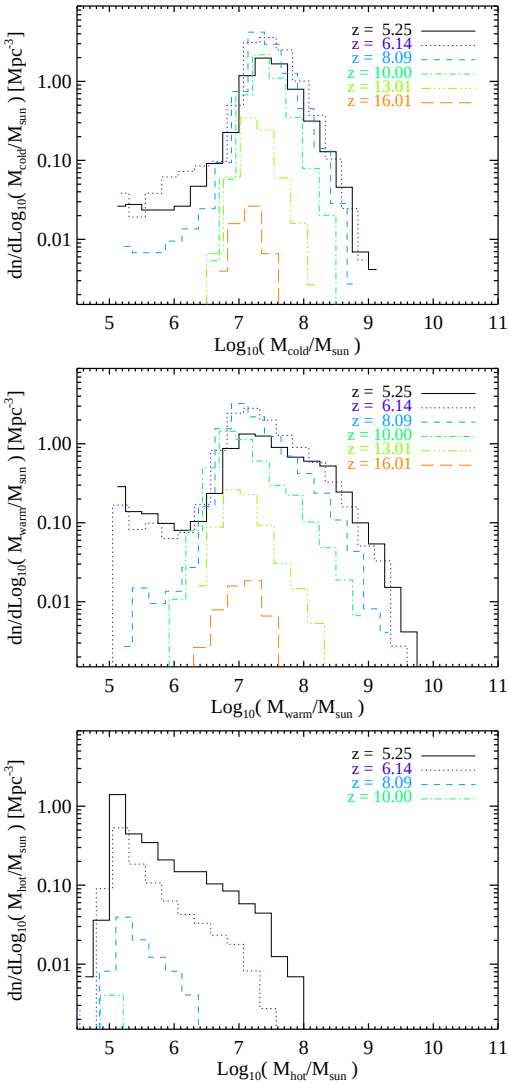



**Fig. 3.** Cold (top), warm (centre), and hot (bottom) gas mass functions at $z$ =5.25, 6.14, 8.09, 10.00, 13.01, and 16.01.

The mass distribution of the young ($t_{\rm age} < 100\,{\rm Myr}$) stellar component is plotted in the bottom panel of Fig. 4 and compared with UV-based determinations for $z = 6$–10 HST and Spitzer galaxies (Stefanon et al. 2021). The resulting trend decreases with $M_{\rm star}$ and follows a Schechter form, while redshift

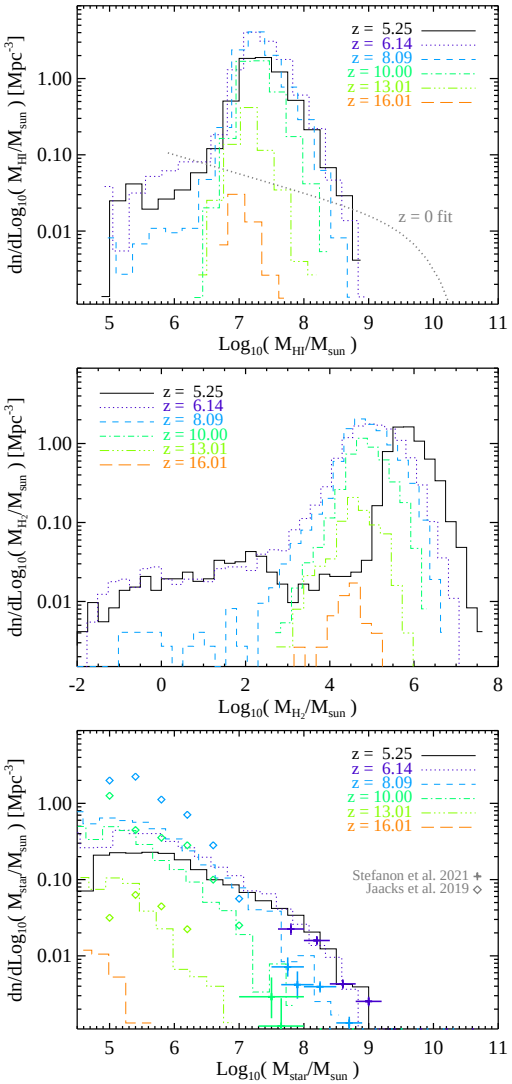



**Fig. 4.** HI (top), $H_2$ (centre),and stellar (bottom) mass functions at different $z$ with a fit to $z = 0$ ALFALFA HI data by Jones et al. (2018) (top panel, dotted grey line), $z = 6$–10 HST/Spitzer masses by Stefanon et al. (2021) (bottom panel, coloured crosses) and expectations by Jaacks et al. (2019) (bottom panel, coloured diamonds).

evolution is evident in the normalisation and reflects the level of star formation activity from early to late times. A plethora of previous works have shown stellar mass functions, such as those in the bottom panel of Fig. 4. Nevertheless, the low-mass regime is still debated and more observational data of faint or normal star-forming galaxies at those epochs are needed to draw definitive conclusions. Broadly speaking, we find a power-law trend down to $M_{\rm star} \sim 10^6\,{\rm M}_\odot$ and a flattening of the distribution at lower $M_{\rm star}$, while the high-mass regime is in line with the data by Stefanon et al. (2021). Independent theoretical results by Jaacks et al. (2019), despite focusing on a smaller-mass range, find a behaviour that is qualitatively similar to ours (although steeper at $z \sim 8$), with a mild flattening around $M_{\rm star} \sim 10^5$-$10^6\,{\rm M}_\odot$. The existing discrepancies could be ascribed to the different stellar-population assumptions, selection effects, or numerical resolution. As is noted therein, the flattening values correspond to the transition between (smaller) $H_2$-cooling haloes and (larger) H-cooling haloes, with implications for cooling efficiencies. Thus, gas cooling is key for the establishment and shape of the early stellar mass function.

### 3.2. Baryon budget, galaxies and the IGM

We explore where different baryon phases are located and their relations with the hosting environment by looking at the mass density parameters in bound structures and in the IGM, as well as their possible correlations with the main galaxy properties.

#### 3.2.1. Mass phases in bound structures and IGM

Mass density parameters in bound structures and the IGM were estimated by selecting the total mass within a distance of $R < R_{\rm vir}$ from halo centres ($\Omega_{\rm bound}$) and the mass lying beyond any $R_{\rm vir}$ ($\Omega_{\rm IGM}$) for each phase. The selected bound mass therefore included both galaxies and their circumgalactic medium (CGM). The share of cold, warm, hot, stellar, HI, and $H_2$ mass phases in bound structures ($\Omega_{\rm bound,cold}$, $\Omega_{\rm bound,warm}$, $\Omega_{\rm bound,hot}$, $\Omega_{\rm bound,stars}$, $\Omega_{\rm bound,HI}$, $\Omega_{\rm bound,H_2}$) and diffuse gas ($\Omega_{\rm IGM,cold}$, $\Omega_{\rm IGM,warm}$, $\Omega_{\rm IGM,hot}$, $\Omega_{\rm IGM,stars}$, $\Omega_{\rm IGM,HI}$, $\Omega_{\rm IGM,H_2}$) are presented in Fig. 5, while corresponding bound-to-cosmic and IGM-to-cosmic mass density ratios are in Appendix D.

The trends for bound objects follow the halo growth during cosmic evolution with little amounts of mass in bound structures at early times and increasingly large amounts of bound mass at later epochs. This is particularly evident for $\Omega_{\rm bound,warm}$, $\Omega_{\rm bound,hot}$, and $\Omega_{\rm bound,stars}$ that increase monotonically with time and signal the build-up of gaseous and stellar content in galaxies. The trend of $\Omega_{\rm bound,cold}$ is affected by reionisation at $z \simeq 6$, when the UV background radiation ionises HI ($\Omega_{\rm bound,HI}$ drops) and slightly boosts $H_2$ in the thin regions of halo peripheries ($\Omega_{\rm bound,H_2}$ gets enhanced). This causes $\Omega_{\rm bound,warm}$ to dominate the baryons in collapsed structures at $z < 6$. When compared to the whole cosmic mass, the resulting $\Omega_{\rm bound}$ values are different from those in Fig. 2 and discrepancies reach a few dex (consistently with the phase average evolution shown in Appendix D, Fig. D.2).

For the diffuse gas, the values of $\Omega_{\rm IGM,cold}$, $\Omega_{\rm IGM,warm}$, and $\Omega_{\rm IGM,hot}$ tightly follow the corresponding $\Omega_{\rm cold}$, $\Omega_{\rm warm}$, and $\Omega_{\rm hot}$ cosmic behaviour and the picture arising from Fig. 5 is similar to the one of Fig. 2. In the IGM case, the stellar phase is negligible, as primordial stars are typically formed in bound structures (early galaxies). While HI traces IGM cold gas well, $H_2$ features a resulting $\Omega_{\rm IGM,H_2} \sim 10^{-6}$ at $z \simeq 18$ (in line with primordial abundances) and $\Omega_{\rm IGM,H_2} \gtrsim 10^{-5}$ at $z < 6$.

#### 3.2.2. Phase relations

It is debated whether gas phases correlate with the main galaxy properties and if they could be used to infer unknown quantities.

To address these questions, we check gas scaling relations in Fig. 6, where cold, warm and hot gas masses in bound structures are plotted against the hosting $M_{\rm star}$ (upper row) and SFR (lower row). Corresponding mass fractions are shown in Appendix D. To better guide the eye, we overplot fits to simulation results, as reported in Appendix F. Gas phase masses generally increase with $M_{\rm star}$ and SFR and the results in the figure show that the hot component is subdominant by a factor of $\sim 10^2$–$10^3$ at all $z$. Warm and cold phases share comparable amounts of mass with slightly more cold gas in smaller systems ($M_{\rm star} \lesssim 10^7\,{\rm M}_\odot$). The trend is shallower for the cold material and steeper for the warm one (which dominates at SFR $\gtrsim 0.01$–$0.1\,{\rm M}_\odot$). Simulation

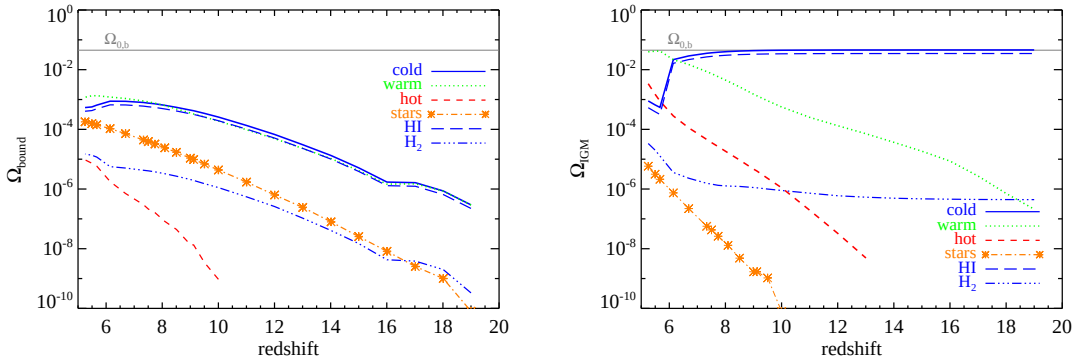



**Fig. 5.** Baryon density parameters in bound objects (left) and the IGM (right) as function of redshift for cold (solid lines), warm (dotted lines), hot (short-dashed lines), stellar (dot-dashed lines with asterisks), HI (long-dashed lines), and $H_2$ (dot-dot-dot-dashed lines) phases. The horizontal grey line marks the value of $\Omega_{0,b}$. Stars form out of cold gas that dominates the baryon budget at $z \gtrsim 6$ and is overtaken by warm gas at later times.

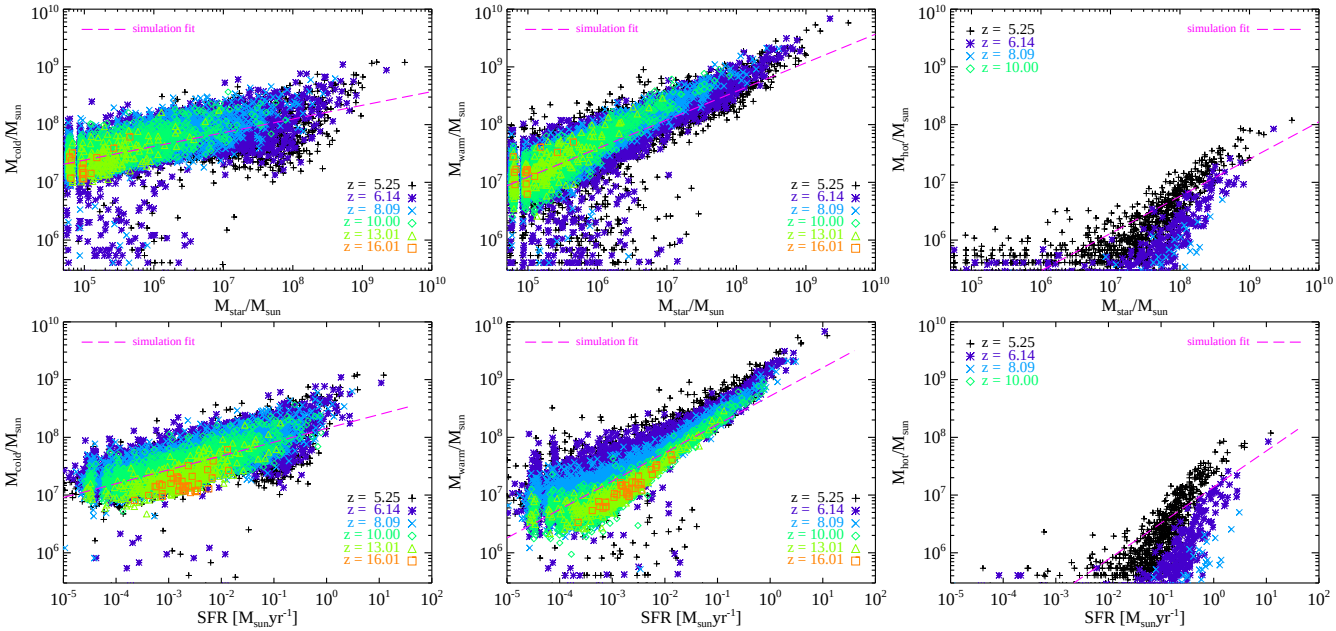



**Fig. 6.** Cold (left column), warm (central column), and hot (right column) gas mass versus $M_{star}$ (top row) and SFR (bottom row) for galaxies at redshift $z$ = 5.25, 6.14, 8.09, 10.00, 13.01, and 16.01, with simulation fits (dashed magenta lines) reported in Appendix F (Table F.1). Different gas phases probe different $M_{star}$ and SFR regimes with little redshift evolution, but a large environment and feedback-driven scatter.

results suggest that cold, warm and hot gas masses increase with both $M_{star}$ and SFR with slopes of ∼0.2, 0.5 and 0.6 (Table F.1).

We further explore the trends of HI and $H_2$ masses as functions of $M_{vir}$, $M_{star}$, and SFR in Fig. 7. We compare our predictions with $z \sim 0$ HI data from HIPASS and ALFALFA surveys (Padmanabhan & Kulkarni 2017; Guo et al. 2021) and with $H_2$ data from ALMA/NOEMA surveys of star-forming galaxies at $z \sim 1$–3 (Bertola et al. 2024), nearby DustPedia galaxies (Salvestrini et al. 2025), and MUSE-ALMA galaxies (Bollo et al. 2026). HI and $H_2$ mass relations feature little evolution and the scatter broadens due to both larger sample statistics and increasing feedback impacts at lower $z$. Their scalings with $M_{star}$ and SFR are similar, consistently with the main-sequence relation at this epoch, and are characterised by slopes of roughly 0.2 and 0.5 (Table F.2). The $H_2$ behaviour is in agreement with recent MUSE-ALMA upper limits at $z \simeq 0.5$ by Bollo et al. (2026) and the fundamental plane by Salvestrini et al. (2025), whose multi-parametric fit suggests an $M_{H_2}$-SFR slope of 0.51 at $z \simeq 0$ (see also Sargent et al. 2014). Low-$z$ observations are qualitatively in line with our predictions, although they bear remarkable uncertainties (Romeo 2020; Romeo et al. 2020; Chowdhury et al. 2022; Bianchetti et al. 2025).

Supplementary material about HI and $H_2$ total gas fractions $f_{HI}$ and $f_{H_2}$ versus $M_{vir}$, $M_{star}$, SFR, and $Z$ is given in Appendix D. Here, we only stress that, due to feedback effects, $f_{HI}$ may reach values $\lesssim$0.1 of the whole gas mass (in objects dominated by warm or hot gas), while $f_{H_2}$ is typically around a few percent, but reaches values larger than 10% in cold, metal-enriched, star-forming sites. Finally, we checked the relations between gas phases and metallicities and found that they are similar to the ones in Figs. 6 and 7 because of the mass-metallicity relation.

### 3.3. Baryon cycling: Connecting gas and stars

Baryon phases are influenced by both the stellar activity – that returns a fraction of stellar mass to the gaseous environment during stellar evolutionary stages (stellar return

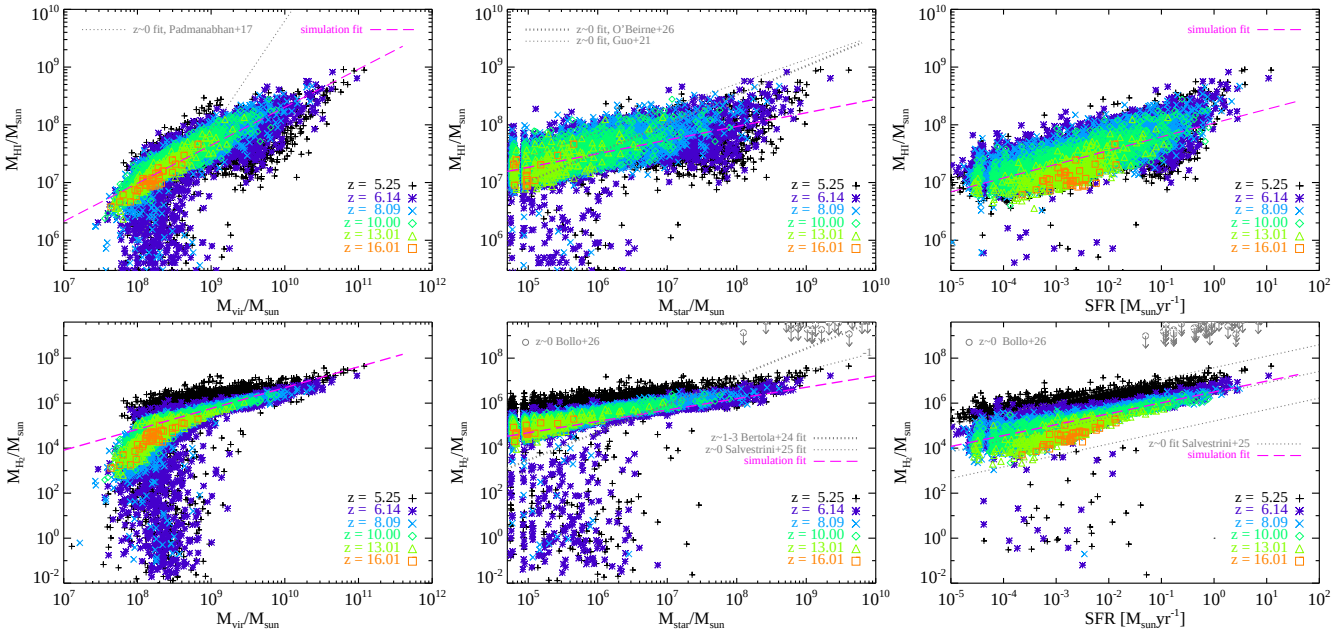



**Fig. 7.** HI (top) and $H_2$ (bottom) masses versus $M_{vir}$ (left), $M_{star}$ (centre), and SFR (right). Observational fits for HI and $H_2$ data are shown by grey dotted lines and MUSE-ALMA Haloes $H_2$ upper limits (Bollo et al. 2026) by grey circles and arrows. The fit to the MUSE-ALMA Haloes $M_{HI}$ vs. $M_{star}$ is $\mathrm{Log}(M_{HI}/M_\odot) = 0.50\,\mathrm{Log}(M_{star}/M_\odot) + 4.52$ (O'Beirne et al. 2026, priv. comm.) and is extrapolated from galaxy data at $M_{star} \sim 10^8$–$10^{12}\,M_\odot$. Multi-parametric fits by Salvestrini et al. (2025) are shown for SFR $= 10^{-1}\,M_\odot\,yr^{-1}$ (lower central panel) and $M_{star} = 10^{8.5}, 10^7$, and $10^{5.5}\,M_\odot$ (dotted lines from top to bottom in the lower right panel). Simulation fits (dashed magenta lines) are in Appendix F (Table F.2). Results are little dependent on redshift and feature a large environment-driven scatter.

fraction; $R$) – and the efficiency with which gas is converted into stars during a typical depletion time (star formation efficiency; SFE). These two phenomena are signposts of the interaction between gas and stars and we quantify them in the next section.

### 3.3.1. Stellar return fraction

The stellar return fraction, $R$, depends on the assumed stellar IMF, metal yields, mass loss during SN explosions and AGB winds, stellar remnants, and stellar lifetimes. Most authors rely on IMF-integrated averages of $R$, although this can vary for different populations and metallicities. Since in our simulations we track the stellar age ($t_{age}$) of each population and the respective chemical enrichment and mass losses, here we improve on previous estimates by computing $R$ self-consistently at different times for multiple stellar populations. For each output, the average return fraction is $R = 1 - \Omega_{stars}/\Omega_{0,stars}$, with $\Omega_{stars}$ and $\Omega_{0,stars}$ current and initial stellar mass density parameters.

Fig. 8 shows the resulting average trend for $R(t_{age})$ at $z = 5$, 12, and 18, fitted as a function of $t_{age}$ as follows:

$$R(t_{age}) = 0.0885\,\mathrm{Log}\left(\frac{t_{age}}{3.853\,\mathrm{Myr}}\right), \quad (2)$$

if $t_{age} > 3.853$ Myr and $R = 0$ otherwise. We note that, at $t_{age} \simeq 10$ Gyr, $R \simeq 0.3$, consistently with the expectations for a Salpeter IMF.

Our results imply that in high-$z$ galaxies the amount of stellar mass that is released into the surrounding gas is smaller than the amount inferred by common IMF-integrated estimates. Our $z = 5$ figures are around 0.15–0.20, i.e. half of the typically adopted values. This is a consequence of the younger ages

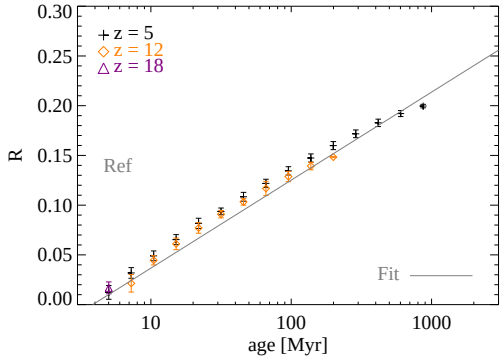



**Fig. 8.** Stellar return fraction $R$ as a function of stellar age for simulated data at redshifts $z = 5$ (crosses) , 12 (diamonds), and 18 (triangles) in the Ref run. Data points refer to median $R$ values with median absolute deviation, while the solid grey line is the corresponding fit (Eq. 2).

in high-$z$ populations that have had not enough time to evolve through all the stellar stages and eject large amount of mass back to the surrounding environment. These considerations suggest that the recycled material affects the baryon budget by a fraction of $\lesssim$20% at $z > 5$ and, since gas phases influenced by star formation feedback are predominantly warm, the corresponding $\Omega_{warm}$ values (in e.g. Fig. 2) would share such recycled baryons at the time of their ejection. On the other hand, early SN and AGB events (that take place on timescales of up to a few hundreds million years) seem efficient at boosting $R$ to levels that are only a factor of two away from late-time expectations. These findings are not severely affected by metallicity effects (Appendix A) and impact available high-$z$ SFRDs, which appear to suffer from $R$ mis-estimates on top of IMF uncertainties (in Table 3).

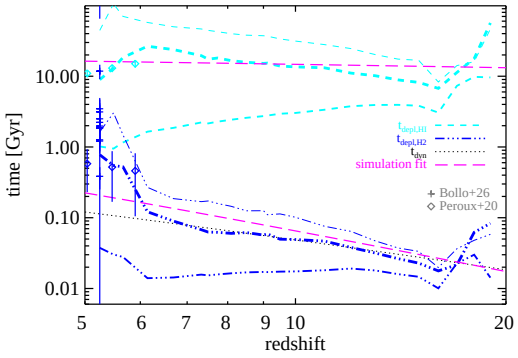



**Fig. 9.** Redshift evolution of average (regular lines), mean (thin lines), and median (thick lines) HI and $H_2$ depletion times compared to dynamical time, $t_{dyn}$ (dotted black line), and observational expectations by Bollo et al. (2026) at low $z$ (crosses with $1\sigma$ dispersion) and Péroux & Howk (2020) at $z \simeq 5$–6 (diamonds with $1\sigma$ dispersion). Simulation fits (Appendix F) are overplotted with long-dashed magenta lines.

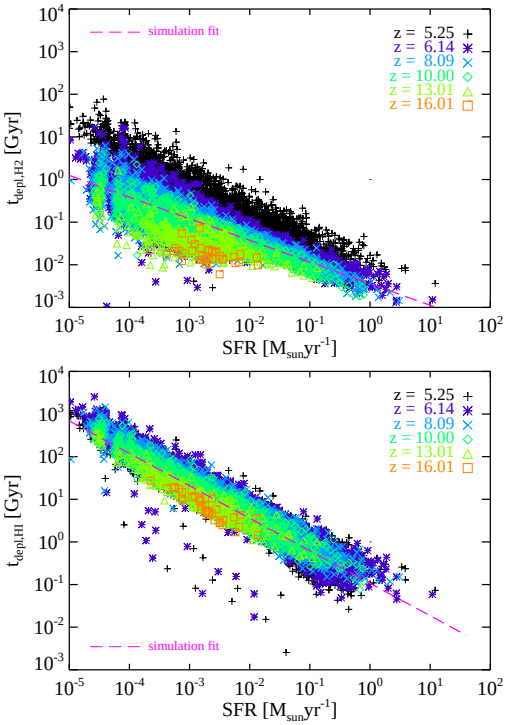



**Fig. 10.** $H_2$ (top) and HI (bottom) depletion times versus SFR at $z$ = 5.25, 6.14, 8.09, 10.00, 13.01, and 16.01 with simulation fits (Appendix F, Table F.3). Further trends with galaxy properties are in Appendix E.

### 3.3.2. Gas depletion and star formation

Depletion times effectively quantify the timescales needed to transfer mass from the cold HI and $H_2$ phases to the stellar phase and are defined as: $t_{depl,HI} = M_{HI}/SFR$ and $t_{depl,H_2} = M_{H_2}/SFR$. In Fig. 9, the average HI depletion time presents an evolution from $t_{depl,HI} \sim 10$ Gyr at $z \sim 20$ to about 1 Gyr at $z \sim 5$. Mean and median values are larger, at variance with the typical Hubble times at those epochs. The values for $t_{depl,H_2}$ lie around ∼0.01–1 Gyr at $z \sim 5$–20. They are shorter than the Hubble time at the same epochs and support the formation of bursty objects at $z \sim 15$ and beyond. Mean and median values may differ from simple averages by a factor of a few up to one dex, as is shown in the figure. As a reference, the fitting expressions for the median HI and $H_2$ trends at $z \simeq 5$–20 are

$$\mathrm{Log}(t_{depl,HI}/\mathrm{Gyr}) = 1.345 - 0.170\,\mathrm{Log}(1+z), \quad (3)$$

$$\mathrm{Log}(t_{depl,H_2}/\mathrm{Gyr}) = 0.943 - 2.045\,\mathrm{Log}(1+z). \quad (4)$$

The latter roughly follows the dynamical time of density contrasts $\Delta \simeq 500$, $t_{dyn} = \pi t_H/\sqrt{2\Delta} \simeq 0.1\,t_H$, with $t_H$ Hubble time (Fig. 9). Fits for average and mean evolution are in Appendix F.

In Fig. 10, $t_{depl,HI}$ and $t_{depl,H_2}$ are plotted as functions of SFR (further relations with $M_{star}$, gas $Z$, and sSFR can be found in Appendix E). Their trend decreases as a result of ongoing star formation activity. In particular, the bulk of $t_{depl,H_2}$ values are about 0.01–0.05 Gyr at $z \simeq 16$ and about 0.1–1 Gyr at $z \simeq 6$. Minimum values are reached in larger ($M_{star} \gtrsim 10^8\,M_\odot$), more star-forming (SFR $> 0.1\,M_\odot\,yr^{-1}$) structures where typical gas metallicities are $Z > 0.01\,Z_\odot$. Because of the $H_2$ sensitivity to star-forming processes, the $t_{depl,H_2}$ scatter is broader than $t_{depl,HI}$ and is due to environment and feedback episodes that alter gas molecular content and cooling capabilities in a non-trivial way. HI trends at different redshifts feature resulting normalisations that are higher by one or two dex. Fits to simulation results demonstrate that HI and $H_2$ depletion times decrease with SFR (stellar mass) with slopes of −0.7 and −0.5 (−0.6 and −0.3), respectively (Table F.3).

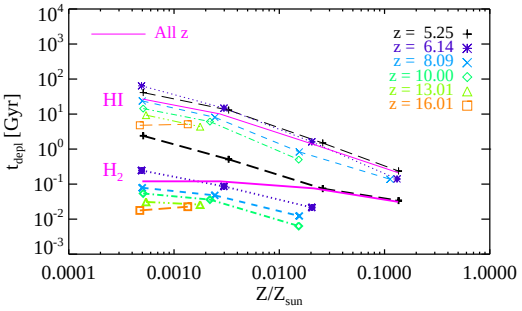



**Fig. 11.** Median HI (thin symbols) and $H_2$ (thick symbols) depletion times vs $Z$ at different $z$ (coloured symbols) and for the whole $z$ range (solid magenta lines). Gas metallicity affects depletion times at all $z$.

In Fig. 11 the median HI and $H_2$ depletion times versus gas metallicity are displayed for the whole redshift range as well as for the different $z$ considered in one-dex metallicity bins. The figures show neatly that average trends are decreasing with gas metallicity as a consequence of more efficient star formation in metal-rich environments. The difference between the average $t_{depl,HI}$ and $t_{depl,H_2}$ is almost three dex at $Z \lesssim 0.001\,Z_\odot$ and one dex at $Z \gtrsim 0.1\,Z_\odot$. This suggests that metals are efficient in lowering $t_{depl,HI}$, although they are less crucial for $t_{depl,H_2}$.

Gas timescales allow us to infer the SFE of a given object, $t_{ff}/t_{depl}$, with $t_{ff}$ and $t_{depl}$ gas free-fall time and depletion time (Fig. 12, top panel). We find a median SFE ∼ 0.01–0.04, and values of around 0.1 for more star-forming objects (SFR $> 0.01\,M_\odot\,yr^{-1}$). This is in agreement with low-$z$ data (Ni et al. 2025) and the lack of evidence for increased SFE at early times (Zavala et al. 2019; Donnan et al. 2025).

Another interesting timescale is the recovery time, $t_{rec}$, which gives the time needed for gas to cool again after being heated by stellar feedback during the initial stages of star formation. We check its role in describing star-forming events in the lower panel of Fig. 12. The values of $t_{rec}$ are functions of SN mass or, equivalently, lifetime ($t_{age}$), and in Appendix F we provide fits to the results by Jeon et al. (2014) in the range of $t_{rec} \sim 9$–300 Myr for

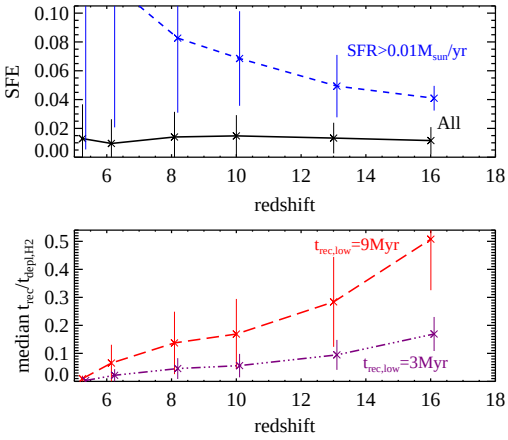



**Fig. 12.** Top: Median SFE redshift evolution with $1\sigma$ spread (top) for all (solid line) and star-forming (short-dashed line) objects. Bottom: Median $t_{\rm rec}/t_{\rm depl,H_2}$ ratios with $1\sigma$ spread for $t_{\rm rec,low} = 9$ Myr (long-dashed line) and 3 Myr (dot-dashed line) lower limits.

15–200 $M_\odot$ SN explosions hosted in a halo with mass $5\times10^5$ $M_\odot$. We adopt the mentioned $t_{\rm rec}$–$t_{\rm age}$ fit in Appendix F and estimate median values of $t_{\rm rec}/t_{\rm depl,H_2}$ for the simulated galaxy population. To bracket uncertainties about $t_{\rm rec}$ lower values ($t_{\rm rec,low}$), we consider both 9 Myr and 3 Myr for $t_{\rm rec,low}$ (in line with Table 1 in Jeon et al. 2014) when using our fit. We find that $t_{\rm rec}$ behaves as a good tracer of the initial episodes of star formation in molecular gas, when it accounts for roughly 20–50% of the $H_2$ depletion time ($z \simeq 16$); however, ongoing feedback effects make its contribution drop down to 1–10% at $z \simeq 5$–6.

## 4. Discussion

This paper presents an analysis of the baryon phases at the epoch of reionisation and, as for any research work, the obtained results may depend on the model assumptions performed, but also give hints as to how to interpret observational findings.

### 4.1. Model assumptions

We considered star particles as simple stellar populations described by a Salpeter IMF, although different choices are possible due to uncertainties in the sampling of low-mass, long-lived stars (see Table 3). We included energy ejection and mass loss from type-II SNe, low-mass stars and intermediate-mass stars. We accounted for type-Ia SNe by considering the classical (favoured) single-degenerate scenario (Whelan & Iben 1973), in which they form in binary systems after a delay of ∼0.1 Gyr and about 50% of them explode within 1 Gyr, irrespectively of the exact delay time distribution (Iben & Tutukov 1994; Greggio 2005; Cappellaro et al. 2015; Maoz & Graur 2017). The properties of the resulting population might depend on the inclusion of stellar rotation and post-zero-age-main-sequence evolution at high $z$, though (Hassan et al. 2025).

Gas cooling takes place via resonant, fine-structure, and molecular lines and is responsible for the transition from hot to warm and cold phases (Maio et al. 2007, 2010), while winds are generated within the smoothing kernel of star-forming particles with a constant velocity of 350 km/s and are decoupled from hydro calculations after their ejection in overdense regions (e.g. Maio et al. 2011a). Different wind implementations could potentially affect the gas located near star-forming sites, but the impacts should be limited as long as wind velocities are kept in realistic ranges, of around a few $10^2$ km/s, and mass loading factors do not exceed extreme values of ∼5 (Perrotta et al. 2024).

We checked resolution effects and found that there can be differences in the warm, hot, and stellar phases, but the resulting trends are similar within one dex or less (Appendix A). This finding is related to the optimal gas resolutions adopted here which allow us to resolve gas phases at scales from megaparsecs to tens of parsecs at $z \gtrsim 10$. This is consistent with previous works (Creasey et al. 2011) that demonstrated that numerical overcooling can severely affect results for particle gas masses higher than $\sim10^6$ $M_\odot$. We selected objects by means of their virial mass and number of constituting particles in order to exclude tiny, poorly resolved structures. Different selection criteria (explored in Appendix B) might lead to slightly different results; however, the general trends are preserved.

The temperature thresholds to distinguish cold, warm, and hot gas phases are somewhat arbitrary; however, most literature studies follow the choices we perform here. A typical threshold of $10^4$ K is common in observational investigations to study neutral and HI gas masses at different redshifts (Nelson et al. 2020), while the threshold between warm and hot gas is debated and typically ranges between a few $10^6$ K and $10^7$ K. Here we chose $10^7$ K and note that the impacts of adopting slightly lower values would be limited, due to the large amount of warm mass that dominates over hot gas.

We identified bound and IGM baryons by means of the virial radius. Alternative criteria might impact the final outcomes.

Our results for cosmic mass density parameters demonstrate that cold gas is the main baryon phase until reionisation, when its contribution drops down to $\Omega_{\rm cold} \sim 10^{-3}$ and warm gas takes over. Of course, the details of this transition may depend on the reionisation history, the UV-background model adopted, and assumptions about heating and chemistry rates (Maio et al. 2022). Radiative-transfer effects of the radiation that escapes primordial star-forming regions might have an impact on the actual atomic and molecular abundances, since UV and Lyman-Werner photons might dissociate them in unshielded regions. Due to their rarity, primordial, solar-like, or OB-star sources do not induce dramatic variations in the average HI and $H_2$ content over megaparsec scales (as quantified in Maio et al. 2016).

The sSFR trends we find are in line with observational data (Appendix C); however, caution must be taken when comparing numerical models with observations that may rely on different assumptions about the galaxy main sequence. We neglect primordial black-hole feedback, since in typical conditions its effects are expected to be minor due to the small galaxy masses at these epochs (see further discussion in e.g. Maio et al. 2019).

With these assumptions, our star formation efficiencies are of the order of a few percent, while average stellar return fractions are $R \lesssim 0.2$ at the epoch of interest here (i.e. up to 20% of the initial stellar mass is converted into warm gas). As a consequence, any small fraction of cold gas that forms stars competes with increasing fractions of stellar mass turned back into gas via direct mass loss. These quantities affect the mass transfer from a phase to another; hence, different modelling or theoretical uncertainties of such processes might impact our findings.

We stress that the main thing responsible for the transition of gas from cold to warm or hot phases is not the mass transfer itself, which is quantitatively rather small, but the heating energy produced and injected into the surroundings after such small amounts of gas have formed stars. This happens via SN explosions and feedback, and the differentials of the curves in Figs. 2 and 5 give a quantitative measure of the actual mass

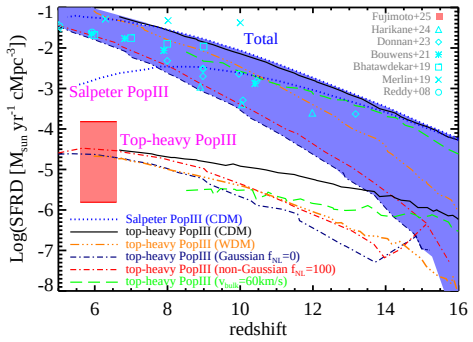



**Fig. 13.** Observed (symbols) and simulated (lines) comoving SFRDs for Salpeter (this work) and top-heavy (previous works) PopIII IMFs and model variations including: CDM and WDM (Maio & Viel 2015, 2023), non-Gaussianities ($f_{\rm NL}$ = 0, 100; Maio & Iannuzzi 2011), and primordial bulk flows at 60 km/s (Maio et al. 2011b). Total SFRDs for different models and resolutions (blue shade) and JWST PopIII determinations (red shade) are also shown. Observational SFRDs are from Reddy et al. (2008), Merlin et al. (2019), Bhatawdekar et al. (2019), Bouwens et al. (2021), Donnan et al. (2023a,b), Harikane et al. (2024), and Fujimoto et al. (2025).

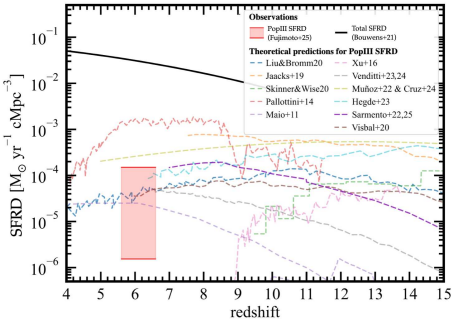



**Fig. 14.** Top-heavy PopIII SFRDs (broken lines) from simulations (Maio et al. 2010, 2011a, Pallottini et al. 2014, Xu et al. 2016, Jaacks et al. 2019, Liu & Bromm 2020, Skinner & Wise 2020, Venditti et al. 2023) and semi-analytical models (Visbal et al. 2020, Muñoz et al. 2022, Hegde & Furlanetto 2023, Sarmento & Scannapieco 2025) compared to total SFRD data (solid line) and JWST PopIII determinations (shaded area) taken from Fujimoto et al. (2025).

transfer. These physical processes lead the mass flows among different phases, determining the complete baryon cycle.

### 4.2. Model variations and implications for the early SFRD

The primordial IMF is particularly debated in the literature (e.g. Palla et al. 1983; Silk 1983; Bromm et al. 2001b; Abel et al. 2002; Tornatore et al. 2007; Maio et al. 2010; Bromm 2013; Liu & Bromm 2020; Klessen & Glover 2023, and references therein) and a top-heavy shape is commonly adopted for PopIII regimes, following prescriptions by Larson (1998). His argument was based on the higher Jeans (Bonnor-Ebert) masses expected at higher redshift, due to the increasing cosmic-background temperature. Subsequent studies have highlighted the role of further physical processes, such as local gas shielding, partial recombination, magnetic fields and binary or cluster formation, which would bring proto-stellar seed masses down to values comparable to solar and following a power-law (unbiased) distribution (Yoshida et al. 2007; Clark et al. 2011; Greif et al. 2011; Hirano et al. 2014; Stacy et al. 2022; Chon et al. 2022; Machida et al. 2025; Gjergo et al. 2026). Direct evidence is not available yet, and thus the PopIII IMF remains unknown.

To test its impacts on the early SFRD, in Fig. 13 we collect our expectations for different model variations, including Salpeter and top-heavy PopIII IMFs in our Ref box, and changes in the background matter density field in different cosmic volumes, such as: warm darm matter (WDM), non-Gaussianities (as parameterised by the $f_{\rm NL}$ parameter, where $f_{\rm NL}$ = 0 is the Gaussian case), and high-order corrections to linear theory inducing coherent megaparsec-scale gas bulk valocities of $v_{\rm bulk}$ = 60 km/s at $2\sigma$ levels (Maio et al. 2011b; Maio & Iannuzzi 2011; Maio & Viel 2015, 2023). While the total SFRDs are similar and suffer mostly from uncertainties in volume sampling or resolution (blue shade), different PopIII IMFs neatly determine different PopIII SFRDs and affect the timing of metal enrichment, photon production, and massive-black-hole formation (Maio et al. 2011a, 2016, 2019; Ma et al. 2017). Changes in the background (WDM, $f_{\rm NL}$ = 100 or $v_{\rm bulk}$ cases) produce limited impacts on PopIII SFRDs, whose trends are still consistent with the latest JWST PopIII constraints at $z \simeq 6$ (Fujimoto et al. 2025). This demonstrates that the effects of alternative cosmological scenarios are subdominant with respect to baryon modelling (Maio et al. 2011a,b, 2012; Maio & Viel 2015, 2023; Pillepich et al. 2018; Villaescusa-Navarro et al. 2021; D'Souza & Bell 2022; Zang & Zhu 2024; Barberi Squarotti et al. 2024; Despali et al. 2025; Acharya et al. 2025; D'Eramo et al. 2025).

Fig. 14 summarises the behaviour of the PopIII SFRD for additional models in the literature. The heterogeneity of theoretical results suggests that current uncertainties or degeneracies are still remarkable, almost two dex ($z \simeq 6$) or larger ($z > 6$), and a definitive consensus must still be reached.

### 4.3. Comparison with the literature

Drawing precise conclusions based on direct comparisons with observations at the epochs of interest here is not trivial and quantification of early gas phases is still an open problem. Observational determinations of stellar masses are difficult (one-dex error), as well as HI mass estimates, while $H_2$ values rely on indirect (CO) low-$z$ calibrations. Detections of kiloparsec-scale [CII] emission up to $z \simeq 7$ are consistent with the existence of significant amounts of cold gas in primordial sources (Bischetti et al. 2024; Zanella et al. 2024; Decarli & Díaz-Santos 2025; Algera et al. 2025; Narita et al. 2026; Vizgan et al. 2026; Chiang 2026), in line with our conclusions. There seems to be growing evidence of $z > 6$ cold outflows detected via $OH^+$ 290 μm and OH 119 μm absorption lines tracing atomic diffuse gas and dense molecular gas, respectively (e.g. ALMA detections by Shao et al. 2022, Salak et al. 2024, and Spilker et al. 2025).

Qualitatively speaking, given the remarkable differences we find between the trends of the cosmic Ω parameters and the $\Omega_{\rm bound}$ ones, one must conclude that estimates of the baryon budget based on the mass of bound structures could be biased and recent $\Omega_{\rm HI}$ results by Oyarzún et al. (2025) go in this direction.

In large numerical simulations, $H_2$ fractions estimated at post-processing seem to be almost insensitive to the sub-grid models adopted; however, in such analysis the cold and molecular phases cannot be directly traced due to the poor ISM physics (Ward et al. 2022, and references therein). $H_2$ can be further explored through semi-analytical prescriptions calibrated with the present-day observed galaxy populations (Lagos et al. 2015, 2020; Diemer et al. 2018; Davé et al. 2019; Jin et al. 2021;

Szakacs et al. 2022), but this approach tends to underestimate higher-$z$ molecular masses by a factor of a few.

During the cosmic stellar-mass build-up, the amount of the mass returned to the gas phases evolves non-linearly, since the formation of stars is accompanied by a stellar return fraction, $R$, that grows with stellar age (Fig. 8). Although consistent with IMF and stellar-mass uncertainties (Table 3), dependences of $R$ on stellar metallicity (Appendix A) are less severe than what is derived from analytic calculations assuming fixed metallicities (Calura et al. 2014; Vincenzo et al. 2016). More detailed analyses based on simulations that include stellar evolution, time-dependent metal spreading, and feedback mechanisms (such as the one we perform here) are still lacking in the literature.

Baryon mass functions at different $z$ show a variety of trends with typically decreasing high-mass tails. This is somehow reminiscent of the Schechter formalism, but with more complex behaviour at the low-mass end. When comparing our results to observations of the HI mass function at $z \simeq 0$ by Jones et al. (2018), we see that low-$z$ determinations are smoother and extend towards higher HI masses. This highlights a clear redshift evolution of gas mass distributions.

Baryon phases in bound objects are linked to the main galaxy properties, such as mass, SFR, and metallicity, while dependencies of our results on the specific SFR are usually weak, consistently with recent theoretical findings about early fine-structure line emission (Bisbas et al. 2022; Casavecchia et al. 2024, 2025; Muñoz-Elgueta et al. 2024; Nyhagen et al. 2025; Nakazato et al. 2026). In general, cold, warm, and hot gas masses increase with hosting $M_{\rm star}$, SFR, and gas $Z$ and the found relations bare a scatter of one or two dex, as a consequence of star formation stochasticity (Katz et al. 1996). Thus, tight observational correlations might be sample-biased and capture only the trends of more powerful sources, mostly at high redshift.

The broad scatter in the gas phases is reflected in the depletion times. Observational determinations for star-forming galaxies at $z \sim 0$ suggest gas depletion times of ∼2–8 Gyr (Tumlinson et al. 2017) decreasing within $M_{\rm star} \sim 10^{8.5}$–$10^{11.5}\,{\rm M}_\odot$. First surveys of molecular gas in PHIBSS cosmic-noon star-forming galaxies (Tacconi et al. 2013, 2018) found $t_{\rm depl,H_2} \propto (1+z)^{-0.6}$, well approximated by $t_{\rm dyn} \simeq t_{\rm H}/10$. Recent estimates inferred by QSO and main-sequence galaxy observations at $z \simeq 6-7$ suggest $t_{\rm depl,H_2} \sim 0.01$–$0.1$ Gyr (Zavala et al. 2022; Salvestrini et al. 2025), in line with our results. We find that depletion times depend on redshift, but, when averaged over the $z \gtrsim 5$ range, median $t_{\rm depl,H_2}$ values are weakly dependent on gas metallicity and lie around 100 Myr as a result of turbulent (Sabbi et al. 2022), feedback-regulated star formation. Such short $H_2$ timescales make the formation of Milky Way progenitors possible at $z \gtrsim 6$ (Rusta et al. 2024). Corresponding SFEs are around 0.01–0.04 and do not evolve significantly. In this respect, recent findings in isolated-galaxy simulations by Polzin et al. (2024) are in line with ours.

Overall, the theoretical timescales we find in primordial epochs help us understand the first phases of cosmic star formation and the role of feedback and environment in shaping the early baryon cycle. Furthermore, the impact of star formation heating explains why absorption-selected galaxies (e.g. Bollo et al. 2026) are often inefficient at converting cold gas into stars, despite their sizeable molecular reservoir.

### 4.4. Observational insights

From an observational point of view, measurements of $M_{\rm H_2}$ and $M_{\rm star}$ can be inferred from millimetre and optical observations, while $M_{\rm HI}$ is becoming available at cosmological distances thanks to 21 cm detections. For this reason, the following definitions of observational HI and $H_2$ gas-to-star mass fractions and baryon mass fraction are commonly adopted: $\mu_{\rm HI} = M_{\rm HI}/M_{\rm star}$, $\mu_{\rm H_2} = M_{\rm H_2}/M_{\rm star}$ and $F_{\rm gas} = M_{\rm H_2}/(M_{\rm H_2} + M_{\rm star}) = \mu_{\rm H_2}/(\mu_{\rm H_2} + 1)$.

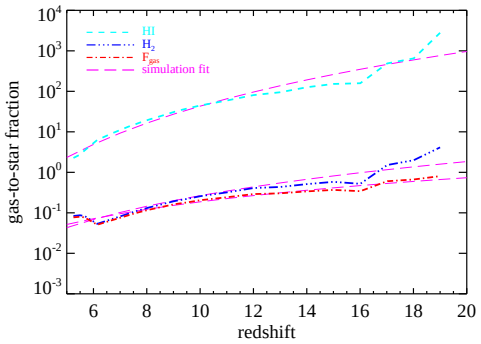



**Fig. 15.** Average $\mu_{\rm HI} = M_{\rm HI}/M_{\rm star}$ (short-dashed line), $\mu_{\rm H_2} = M_{\rm H_2}/M_{\rm star}$ (dot-dot-dot-dashed line), and $F_{\rm gas} = \mu_{\rm H_2}/(\mu_{\rm H_2} + 1)$ (dot-dashed line) redshift evolution with simulation fits (long-dashed lines; Appendix F).

Fig. 15 displays the evolution of the average $\mu_{\rm HI}$, $\mu_{\rm H_2}$, and $F_{\rm gas}$ in the first gigayear. HI gas-to-star fractions decrease monotonically from $\mu_{\rm HI} \sim 10^3$ at $z \gtrsim 20$ down to unity at $z \simeq 5$, while corresponding $\mu_{\rm H_2}$ values range from a few to 0.1. These trends are due to the tiny amounts of stars formed in early epochs in comparison to the dominant cold-gas mass. Subsequent stellar-mass growth and the associated feedback mechanisms cause a shallower evolution of cold-gas phases and a regular decrease in both $\mu_{\rm HI}$ and $\mu_{\rm H_2}$. The $F_{\rm gas}$ behaviour is analogous to $\mu_{\rm H_2}$ with values ranging between ∼0.1 ($z \simeq 5$) and 1 ($z \simeq 20$).

In Fig. 16 we present the dependencies of $\mu_{\rm HI}$, $\mu_{\rm H_2}$, and $F_{\rm gas}$ with $M_{\rm star}$ and corresponding fitting relations for the whole simulated data sample (Table F.2). Observational fractions decrease with $M_{\rm star}$. In particular, the relation between $\mu_{\rm HI}$ and $M_{\rm star}$ is fitted by $\mu_{\rm HI} = 10^{6.08}(M_{\rm star}/M_\odot)^{-0.76}$, and the resulting normalisation and slope are roughly constant in $z$. HI measurements from ALFALFA, GASS, COLDGASS, and xGASS data (Brown et al. 2015; Saintonge et al. 2016; Catinella et al. 2018; Guo et al. 2021) show similar slopes, of between −0.85 and −0.90. However, optically dark sources with a low surface brightness are also detected in HI and lie off the relation at $M_{\rm star} \lesssim 10^7\,{\rm M}_\odot$ (see recent WALLABY results by O'Beirne et al. 2025).

Our expectations for $\mu_{\rm H_2}$ feature a slope ranging between −0.3 (at $z \simeq 16$) and −0.7 (at $z \simeq 5$) and give $\mu_{\rm H_2} \propto M_{\rm star}^{-0.49}$ as average scaling. That broadly agrees with low-$z$ observational results from, for example, xCOLDGASS field galaxies (Saintonge et al. 2017), EDGE-CALIFA spiral galaxies (Bolatto et al. 2017), SDSS star-forming galaxies (Popesso et al. 2020), GASP jellyfish galaxies (Moretti et al. 2023), and PHIBBS, ASPECS, and ALMA/NOEMA galaxies and cosmic-noon AGNs (Bertola et al. 2024) that similarly span a range of a few dex and feature a decreasing $\mu_{\rm H_2}$. The exact slope of the $\mu_{\rm H_2}$–$M_{\rm star}$ relation is still debated. For example, the analysis by Tacconi et al. (2018) is compatible with a slope of −0.33 at $z \sim 0$, while Bertola et al. (2024) find a slope of −1 at cosmic noon, without strong differences between AGN hosts and non-active galaxies. It is unclear whether this is due to possible redshift effects; however, Papastergis et al. (2012) and Peeples et al. (2014) find trends analogous to ours, with $z \sim 0$ gas-to-star ratios in the range 0.1–100 and a slope between −0.48 and −0.43 using measurements by McGaugh (2005, 2012), Leroy et al. (2008) and Saintonge et al. (2011).

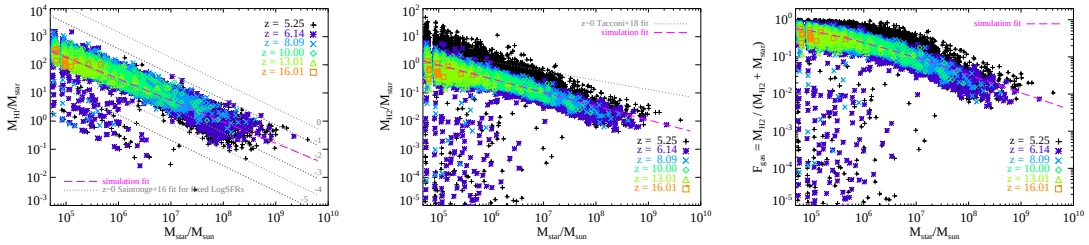



**Fig. 16.** Gas-to-star fractions, $\mu_{\rm HI}$ (left), $\mu_{\rm H_2}$ (centre), and $F_{\rm gas} = \mu_{\rm H_2}/(1+\mu_{\rm H_2})$ (right) as functions of $M_{\rm star}$ compared to $z \simeq 0$ observational fits (dotted lines) for main-sequence galaxies (Saintonge et al. 2016, 2017; Tacconi et al. 2018). Different dotted lines in the left panel correspond to fixed Log(SFR/$M_\odot$ yr$^{-1}$) = 0, –1, –2, –3, –4, and –5, from top to bottom. Dashed magenta lines refer to simulation fits (Appendix F, Table F.2).

Our predictions for $F_{\rm gas}$ suggest typical values of between 0.1 and 0.8 for most of the sampled stellar masses and a drop below 10% at more massive scales. The trend has an average slope of roughly −0.3; however, it is better fitted by the $\mu_{\rm H_2}$-based relation $F_{\rm gas} = [1+0.0036\,(M_{\rm star}/{\rm M}_\odot)^{0.49}]^{-1}$. In the figure, scattered data points below $\mu_{\rm HI}$, $\mu_{\rm H2}$, and $F_{\rm gas}$ trends represent galaxies that are either inactive or that have suffered outflow-driven HI and $H_2$ mass removal. The $F_{\rm gas}$ bending reflects environment or feedback-induced molecular suppression and might be at the origin of the SFR-$M_{\rm star}$ bending at later time (Popesso et al. 2019; Pérez-Martínez et al. 2025). Estimates for nearby resolved galaxies observed with Hershel agree with typical $F_{\rm gas} \simeq 0.04$ and range between 0.02 and 0.6 depending on metallicity and dust content (Casasola et al. 2022). NOEMA determinations of $z < 1$ $H_2$-cooling bright central galaxies yield $F_{\rm gas} \simeq 0.1$–0.5 (Castignani et al. 2025). At $z \simeq 1$–5, observations of star-forming gas have been reporting routinely $F_{\rm gas} \simeq 0.3$–0.8 (Daddi et al. 2010; Saintonge et al. 2011; Harris et al. 2012; Magnelli et al. 2012; Tacconi et al. 2013; Bothwell et al. 2013; Scoville et al. 2016) and studies of resolved molecular gas in $z \simeq 2$–3 lensed active galaxies suggest $F_{\rm gas} \simeq 0.6$ (Spingola et al. 2020). Recent analysis of ALMA/SDSS $z \simeq 2$ quasars (Molyneux et al. 2025) agree with $F_{\rm gas} \simeq 0.02$–0.24 ($\mu_{\rm H_2} \simeq 0.02$–0.32). Values from $z \sim 4$–8 primordial galaxies show $F_{\rm gas} \simeq 0.3$–0.9 (Dessauges-Zavadsky et al. 2020; Heintz et al. 2023; Aravena et al. 2024; Fudamoto et al. 2025). At higher $z$ there is no convergence, yet, and upper limits at $z \simeq 14$ range between 0.5 (Helton et al. 2025b) and 0.8 (Schouws et al. 2025b; Carniani et al. 2025).

All these observational results together with the expected large theoretical scatter are in line with the idea that high-$z$ star-forming galaxies might be more gas-rich than present-day ones due to their more limited evolution. Environment or dynamical conditions (mass, SFR, $Z$, mergers) do play a relevant role and induce significant variations in the actual abundances (as observationally suggested at lower $z$ by e.g. Kanekar et al. 2018; Donevski et al. 2020; Zanella et al. 2023, 2026); hence, HI and $H_2$ do not necessarily fill up the whole galaxy gas budget. The warm component can account for more than 50% of the gas content in bound structures and HI and $H_2$ mean fractions can reach values as low as 0.2 and $10^{-3}$, respectively (Appendix D). Hints about the role of warm cosmic gas are also suggested by low-$z$ H Ly$\alpha$ studies (Viel et al. 2017; Scarlata et al. 2025; Gelli et al. 2025; Rowland et al. 2025) and partially ionised atomic species, such as OVI or CIV (Peeples et al. 2014; Werk et al. 2019; Lochhaas et al. 2025). Also MgII, NII, and OIII lines are diagnostics of mildly warm gas and have been recently detected at high $z$ (Hennawi et al. 2021; Kolupuri et al. 2025; Perna et al. 2025; Belladitta et al. 2025; Nakazato et al. 2026), but a reliable quantification has proven to be difficult. For hot gas, the situation is much more uncertain, as $T > 10^7$ K gas is mostly detected in low-$z$ galaxy groups and clusters via X-ray emission. While hot-gas fractions can be related to total mass in both simulations and observations at $z < 1$ (Comparat et al. 2023; Zhang et al. 2024a,b; Rasia et al. 2025; Marini et al. 2025; Biffi et al. 2025), the high-$z$ regime still deserves investigations. In addition, the spread among available observations is ∼dex, due to the different data (XMM-Newton, Chandra, SZ, gravitational lensing), selections (X-ray or optical), or assumptions (hydrostatic equilibrium, scaling relations) adopted to retrieve the hot mass.

## 5. Conclusions

In this work we have exploited the up-to-date ColdSIM numerical simulations to make predictions about the baryon budget of early galaxies and explore correlations that may be used to infer unknown quantities. We implemented detailed non-equilibrium chemistry of several chemical species, which guaranteed that HI and $H_2$ abundances were traced consistently with metal-dependent cooling, heating, and feedback processes during cosmic structure evolution. This allowed us to explicitly follow the cold, warm, and hot gas thermal phases without relying on poorly constrained sub-grid assumptions. Our findings can be summarised as follows.

- Baryon mass density parameters at $z > 5$ are dominated by gas, both in bound structures (galaxies/CGM) and in the IGM, and bound objects contain only a small fraction of the entire baryonic mass, around $10^{-6}$–$10^{-2}$.
- The cold phase dominates the epoch of reionisation, but warm gas is present by $z \sim 20$ and increases with time, taking over the cosmic baryon budget at $z \lesssim 6$.
- Due to uncertainties in the adopted IMF, the stellar-mass density parameter can vary within 0.3 dex.
- Phase mass functions evolve with $z$ and show feedback-driven trends at low masses and a more regular Schechter-like shape at the high-mass end.
- Gas phases correlate with the host galaxy $M_{\rm star}$ and SFR, and feature a more scattered behaviour with gas $Z$.
- HI traces the whole cold phase fairly well, while $H_2$ gas is tightly linked to star formation with $t_{\rm depl,H_2} \sim 0.01$–0.1 Gyr.
- Typical $t_{\rm depl,HI}$ and $t_{\rm depl,H_2}$ decrease with $M_{\rm star}$ and SFR and correlate weakly with $Z$.
- Median star formation efficiencies are around a few percent and do not evolve significantly with redshift.
- The stellar return fraction increases up to $R \simeq 0.2$ for $t_{\rm age} \simeq 1$ Gyr (a factor of two lower than the values commonly adopted) and this impacts high-$z$ SFRDs.
- Observation-based $\mu_{\rm HI}$, $\mu_{\rm H_2}$, and $F_{\rm gas}$ fractions show decreasing trends with cosmic time, $M_{\rm star}$, and SFR, but cannot be considered as fair proxies of the whole galaxy gas content.

– Matter phases and depletion times are related to host galaxy properties via simple scaling relations (see the appendix).

*Acknowledgements.* We thank the anonymous referee for constructive comments that allowed us to improve the original manuscript. We are grateful to V. Bollo and T. O'Beirne for useful discussions and for kindly sharing MUSE-ALMA Haloes data and to S. Fujimoto and R. P. Naidu for granting leave to reproduce their PopIII data collection. UM expresses gratitude to the Italian National Institute of Astrophysics for financial support provided through Theory Grant no. 1.05.23.06.13 "FIRST – First Galaxies in the Cosmic Dawn and the Epoch of Reionisation with High Resolution Numerical Simulations" and Travel Grant no. 1.05.23.04.01. UM also acknowledges warm hospitality at the European Southern Observatory during the completion of this work and motivating interactions with Camilla Maio. We finally acknowledge the NASA Astrophysics Data System and the JSTOR archive for their bibliographic tools.

## References

Abel, T., Anninos, P., Zhang, Y., & Norman, M. L. 1997, New Astron., 2, 181
Abel, T., Bryan, G. L., & Norman, M. L. 2002, Science, 295, 93
Acharya, A., Ma, Q.-B., Giri, S. K., et al. 2025, MNRAS
Algera, H. S. B., Herrera-Camus, R., Aravena, M., et al. 2025, A&A, submitted [arXiv:2512.02320]
Aravena, M., Heintz, K., Dessauges-Zavadsky, M., et al. 2024, A&A, 682, A24
Bacchini, C., Fraternali, F., Iorio, G., & Pezzulli, G. 2019, A&A, 622, A64
Bacchini, C., Nipoti, C., Iorio, G., et al. 2024, A&A, 687, A115
Bañados, E., Khusanova, Y., Decarli, R., et al. 2024, ApJ, 977, L46
Barberi Squarotti, M., Camera, S., & Maartens, R. 2024, JCAP, 2024, 043
Becker, G. D., Bolton, J. S., & Lidz, A. 2015, PASA, 32, e045
Becker, G. D., Bolton, J. S., Zhu, Y., & Hashemi, S. 2024, MNRAS, 533, 1525
Behroozi, P., Wechsler, R. H., Hearin, A. P., & Conroy, C. 2019, MNRAS, 488, 3143
Bell, E. F., & de Jong, R. S. 2001, ApJ, 550, 212
Bell, E. F., McIntosh, D. H., Katz, N., & Weinberg, M. D. 2003, ApJS, 149, 289
Belladitta, S., Bañados, E., Xie, Z.-L., et al. 2025, A&A, 699, A335
Bertola, E., Circosta, C., Ginolfi, M., et al. 2024, A&A, 691, A178
Bhatawdekar, R., Conselice, C. J., Margalef-Bentabol, B., & Duncan, K. 2019, MNRAS, 486, 3805
Bianchetti, A., Sinigaglia, F., Rodighiero, G., et al. 2025, ApJ, 982, 82
Biffi, V., Rasia, E., Borgani, S., et al. 2025, A&A, 698, A238
Bisbas, T. G., Walch, S., Naab, T., et al. 2022, ApJ, 934, 115
Bischetti, M., Choi, H., Fiore, F., et al. 2024, ApJ, 970, 9
Blackwell, A. E., Bregman, J. N., & Davis, S. C. 2026, ApJ, 997, 109
Bolatto, A. D., Wong, T., Utomo, D., et al. 2017, ApJ, 846, 159
Bollo, V., Peroux, C., Zwaan, M., et al. 2026, A&A, 707, A81
Boogaard, L. A., Decarli, R., Walter, F., et al. 2023, ApJ, 945, 111
Bosman, S. E. I., Fan, X., Jiang, L., et al. 2018, MNRAS, 479, 1055
Bothwell, M. S., Aguirre, J. E., Chapman, S. C., et al. 2013, ApJ, 779, 67
Bouwens, R. J., Oesch, P. A., Stefanon, M., et al. 2021, AJ, 162, 47
Bromm, V. 2013, Rep. Prog. Phys., 76, 112901
Bromm, V., Ferrara, A., Coppi, P. S., & Larson, R. B. 2001a, MNRAS, 328, 969
Bromm, V., Kudritzki, R. P., & Loeb, A. 2001b, ApJ, 552, 464
Brown, T., Catinella, B., Cortese, L., et al. 2015, MNRAS, 452, 2479
Calura, F., Ciotti, L., & Nipoti, C. 2014, MNRAS, 440, 3341
Cappellaro, E., Botticella, M. T., Pignata, G., et al. 2015, A&A, 584, A62
Carniani, S., Hainline, K., D'Eugenio, F., et al. 2024, Nature, 633, 318
Carniani, S., D'Eugenio, F., Ji, X., et al. 2025, A&A, 696, A87
Casasola, V., Bianchi, S., Magrini, L., et al. 2022, A&A, 668, A130
Casavecchia, B., Maio, U., Péroux, C., & Ciardi, B. 2024, A&A, 689, A106
Casavecchia, B., Maio, U., Péroux, C., & Ciardi, B. 2025, A&A, 693, A119
Castignani, G., Combes, F., Salomé, P., Edge, A., & Jablonka, P. 2025, A&A, 700, A197
Catinella, B., Saintonge, A., Janowiecki, S., et al. 2018, MNRAS, 476, 875
Ceverino, D., Glover, S. C. O., & Klessen, R. S. 2017, MNRAS, 470, 2791
Chabrier, G. 2003, PASP, 115, 763
Chemerynska, I., Atek, H., Furtak, L. J., et al. 2024, MNRAS, 531, 2615
Chiaki, G., Schneider, R., Nozawa, T., et al. 2014, MNRAS, 439, 3121
Chiang, Y. K. 2026, ArXiv e-prints [arXiv:2602.02658]
Chon, S., Ono, H., Omukai, K., & Schneider, R. 2022, MNRAS, 514, 4639
Chon, S., Hosokawa, T., Omukai, K., & Schneider, R. 2024, MNRAS, 530, 2453
Chowdhury, A., Kanekar, N., & Chengalur, J. N. 2022, ApJ, 941, L6
Cicone, C., Maiolino, R., Sturm, E., et al. 2014, A&A, 562, A21
Cicone, C., Mainieri, V., Circosta, C., et al. 2021, A&A, 654, L8
Clark, P. C., Glover, S. C. O., Klessen, R. S., & Bromm, V. 2011, ApJ, 727, 110
Comparat, J., Luo, W., Merloni, A., et al. 2023, A&A, 673, A122
Conselice, C. J., Adams, N., Harvey, T., et al. 2025, ApJ, 983, 30
Creasey, P., Theuns, T., Bower, R. G., & Lacey, C. G. 2011, MNRAS, 415, 3706
Croton, D. J., Springel, V., White, S. D. M., et al. 2006, MNRAS, 365, 11
Daddi, E., Bournaud, F., Walter, F., et al. 2010, ApJ, 713, 686
Davé, R., Anglés-Alcázar, D., Narayanan, D., et al. 2019, MNRAS, 486, 2827
Davies, F. B., Bosman, S. E. I., D'Odorico, V., et al. 2026, MNRAS, 545, staf1862
Decarli, R., & Díaz-Santos, T. 2025, A&ARv, 33, 4
Decarli, R., Aravena, M., Boogaard, L., et al. 2020, ApJ, 902, 110
Deepak, S., Howk, J. C., Lehner, N., & Péroux, C. 2025, ApJ, 987, 199
D'Eramo, F., Lenoci, A., & Dekker, A. 2025, Phys. Rev. D, 112, 116008
Despali, G., Moscardini, L., Nelson, D., et al. 2025, A&A, 697, A213
Dessauges-Zavadsky, M., Ginolfi, M., Pozzi, F., et al. 2020, A&A, 643, A5
Dev, A., Driver, S. P., Meyer, M., et al. 2024, MNRAS, 535, 2357
Diemer, B., Stevens, A. R. H., Forbes, J. C., et al. 2018, ApJS, 238, 33
Dolag, K., Borgani, S., Murante, G., & Springel, V. 2009, MNRAS, 399, 497
Donevski, D., Lapi, A., Małek, K., et al. 2020, A&A, 644, A144
Donnan, C. T., McLeod, D. J., Dunlop, J. S., et al. 2023a, MNRAS, 518, 6011
Donnan, C. T., McLeod, D. J., McLure, R. J., et al. 2023b, MNRAS, 520, 4554
Donnan, C. T., Dunlop, J. S., McLure, R. J., McLeod, D. J., & Cullen, F. 2025, MNRAS, 539, 2409
D'Souza, R., & Bell, E. F. 2022, MNRAS, 512, 739
Fudamoto, Y., Inoue, A. K., Bouwens, R., et al. 2025, ApJ, submitted [arXiv:2504.03831]
Fujimoto, S., Naidu, R. P., Chisholm, J., et al. 2025, ApJ, 989, 46
Gallazzi, A., Brinchmann, J., Charlot, S., & White, S. D. M. 2008, MNRAS, 383, 1439
Galli, D., & Palla, F. 1998, A&A, 335, 403
Gandolfi, G., Rodighiero, G., Castellano, M., et al. 2025, A&A, 706, A364
Gelli, V., Mason, C., Pallottini, A., et al. 2025, A&A, submitted [arXiv:2510.01315]
Gjergo, E., Zhang, Z., & Kroupa, P. 2026, Res. Astron. Astrophys., in press [arXiv:2601.20998]
Gnedin, N., & Zhu, H. 2025, Open J. Astrophys., 8, 111
Greggio, L. 2005, A&A, 441, 1055
Greif, T. H., Springel, V., White, S. D. M., et al. 2011, ApJ, 737, 75
Guo, H., Jones, M. G., Wang, J., & Lin, L. 2021, ApJ, 918, 53
Harikane, Y., Nakajima, K., Ouchi, M., et al. 2024, ApJ, 960, 56
Harris, A. I., Baker, A. J., Frayer, D. T., et al. 2012, ApJ, 752, 152
Hassan, J. B., Perna, R., Cantiello, M., et al. 2025, ApJ, 992, 68
Hegde, S., & Furlanetto, S. R. 2023, MNRAS, 525, 428
Heintz, K. E., Oesch, P. A., Aravena, M., et al. 2022, ApJ, 934, L27
Heintz, K. E., Giménez-Arteaga, C., Fujimoto, S., et al. 2023, ApJ, 944, L30
Helton, J. M., Alberts, S., Rieke, G. H., et al. 2025a, ApJ, submitted [arXiv:2506.02099]
Helton, J. M., Rieke, G. H., Alberts, S., et al. 2025b, Nat. Astron., 9, 729
Hennawi, J. F., Davies, F. B., Wang, F., & Oñorbe, J. 2021, MNRAS, 506, 2963
Herrera-Camus, R., González-López, J., Förster Schreiber, N., et al. 2025, A&A, 699, A80
Herrmann, K. A., Hunter, D. A., Zhang, H.-X., & Elmegreen, B. G. 2016, AJ, 152, 177
Hirano, S., Hosokawa, T., Yoshida, N., et al. 2014, ApJ, 781, 60
Hollenbach, D., & McKee, C. F. 1979, ApJS, 41, 555
Huertas-Company, M., Shuntov, M., Dong, Y., et al. 2025, A&A, 704, A94
Huyan, J., Kulkarni, V. P., Poudel, S., et al. 2025, ApJ, 991, 228
Iben, I., Jr, & Tutukov, A. V. 1994, ApJ, 431, 264
Jaacks, J., Finkelstein, S. L., & Bromm, V. 2019, MNRAS, 488, 2202
Jeon, M., Pawlik, A. H., Bromm, V., & Milosavljević, M. 2014, MNRAS, 444, 3288
Jiang, J., Fabian, A. C., Dauser, T., et al. 2019, MNRAS, 489, 3436
Jin, S., Dannerbauer, H., Emonts, B., et al. 2021, A&A, 652, A11
Jones, M. G., Haynes, M. P., Giovanelli, R., & Moorman, C. 2018, MNRAS, 477, 2
Kanekar, N., Prochaska, J. X., Christensen, L., et al. 2018, ApJ, 856, L23
Kashino, D., Silverman, J. D., Rodighiero, G., et al. 2013, ApJ, 777, L8
Katz, N., Weinberg, D. H., & Hernquist, L. 1996, ApJS, 105, 19
Kaur, B., Kanekar, N., Neeleman, M., et al. 2025, ApJ, 982, L26
Klessen, R. S., & Glover, S. C. O. 2023, ARA&A, 61, 65
Kolupuri, S., Decarli, R., Neri, R., et al. 2025, A&A, 695, A201
Koribalski, B. S., Crocker, R. M., Khabibullin, I., et al. 2025, PASA, in press [arXiv:2512.15991]
Kroupa, P. 2001, MNRAS, 322, 231
Kulkarni, G., Keating, L. C., Haehnelt, M. G., et al. 2019, MNRAS, 485, L24
Kulkarni, V. P., Bowen, D. V., Straka, L. A., et al. 2022, ApJ, 929, 150
Lagos, C. d. P., Crain, R. A., Schaye, J., et al. 2015, MNRAS, 452, 3815
Lagos, C. d. P., da Cunha, E., Robotham, A. S. G., et al. 2020, MNRAS, 499, 1948
Lamperti, I., Pereira-Santaella, M., Perna, M., et al. 2022, A&A, 668, A45
Langan, I., Popping, G., Ginolfi, M., et al. 2026, A&A, 705, A209
Larson, R. B. 1998, MNRAS, 301, 569

Leroy, A. K., Walter, F., Brinks, E., et al. 2008, AJ, 136, 2782
Liu, B., & Bromm, V. 2020, MNRAS, 497, 2839
Lochhaas, C., Peeples, M. S., O'Shea, B. W., et al. 2025, ApJ, in press [arXiv:2510.25844]
Ma, Q., Maio, U., Ciardi, B., & Salvaterra, R. 2017, MNRAS, 466, 1140
Machida, M. N., Hirano, S., & Basu, S. 2025, ApJ, 988, 6
Madau, P., & Dickinson, M. 2014, ARA&A, 52, 415
Maeder, A. 1992, A&A, 264, 105
Magnelli, B., Saintonge, A., Lutz, D., et al. 2012, A&A, 548, A22
Maio, U., & Iannuzzi, F. 2011, MNRAS, 415, 3021
Maio, U., & Viel, M. 2015, MNRAS, 446, 2760
Maio, U., & Viel, M. 2023, A&A, 672, A71
Maio, U., Dolag, K., Ciardi, B., & Tornatore, L. 2007, MNRAS, 379, 963
Maio, U., Ciardi, B., Dolag, K., Tornatore, L., & Khochfar, S. 2010, MNRAS, 407, 1003
Maio, U., Khochfar, S., Johnson, J. L., & Ciardi, B. 2011a, MNRAS, 414, 1145
Maio, U., Koopmans, L. V. E., & Ciardi, B. 2011b, MNRAS, 412, L40
Maio, U., Salvaterra, R., Moscardini, L., & Ciardi, B. 2012, MNRAS, 426, 2078
Maio, U., Petkova, M., De Lucia, G., & Borgani, S. 2016, MNRAS, 460, 3733
Maio, U., Borgani, S., Ciardi, B., & Petkova, M. 2019, PASA, 36
Maio, U., Péroux, C., & Ciardi, B. 2022, A&A, 657, A47
Malloy, M., & Lidz, A. 2015, ApJ, 799, 179
Maoz, D., & Graur, O. 2017, ApJ, 848, 25
Marini, I., Popesso, P., Dolag, K., et al. 2025, A&A, 698, A191
McGaugh, S. S. 2005, ApJ, 632, 859
McGaugh, S. S. 2012, AJ, 143, 40
Merlin, E., Fortuni, F., Torelli, M., et al. 2019, MNRAS, 490, 3309
Messias, H., Guerrero, A., Nagar, N., et al. 2024, MNRAS, 533, 3937
Molyneux, S. J., Banerji, M., Temple, M. J., et al. 2025, MNRAS, 540, 1163
Moretti, A., Serra, P., Bacchini, C., et al. 2023, ApJ, 955, 153
Moster, B. P., Somerville, R. S., Maulbetsch, C., et al. 2010, ApJ, 710, 903
Muñoz, J. B., Qin, Y., Mesinger, A., et al. 2022, MNRAS, 511, 3657
Muñoz-Elgueta, N., Arrigoni Battaia, F., Kauffmann, G., et al. 2024, A&A, 690, A392
Nagamine, K., Springel, V., & Hernquist, L. 2004, MNRAS, 348, 421
Naidu, R. P., Oesch, P. A., Brammer, G., et al. 2026, Open J. Astrophys., 9, 56033
Nakazato, Y., Sugimura, K., Inoue, A. K., & Ricotti, M. 2026, ApJ, 998, 26
Narita, K., Hatsukade, B., Fujimoto, S., et al. 2026, ApJ, 998, 42
Nasir, F., & D'Aloisio, A. 2020, MNRAS, 494, 3080
Nelson, D., Sharma, P., Pillepich, A., et al. 2020, MNRAS, 498, 2391
Ni, Y., Li, H., Vogelsberger, M., et al. 2025, A&A, 699, A282
Nyhagen, C. T., Schimek, A., Cicone, C., Decataldo, D., & Shen, S. 2025, A&A, 702, A260
O'Beirne, T., Kilborn, V. A., Cluver, M. E., et al. 2025, MNRAS, 544, 1799
Omukai, K., Tsuribe, T., Schneider, R., & Ferrara, A. 2005, ApJ, 626, 627
Oyarzún, G. A., Rafelski, M., Christensen, L., et al. 2025, ApJ, 983, 10
Padmanabhan, H., & Kulkarni, G. 2017, MNRAS, 470, 340
Palla, F., Salpeter, E. E., & Stahler, S. W. 1983, ApJ, 271, 632
Pallottini, A., Ferrara, A., Gallerani, S., Salvadori, S., & D'Odorico, V. 2014, MNRAS, 440, 2498
Papastergis, E., Cattaneo, A., Huang, S., Giovanelli, R., & Haynes, M. P. 2012, ApJ, 759, 138
Parente, M., Bischetti, M., Maio, U., et al. 2026, A&A, 705, A39
Peeples, M. S., Werk, J. K., Tumlinson, J., et al. 2014, ApJ, 786, 54
Pérez-Martínez, J. M., Dannerbauer, H., Emonts, B. H. C., et al. 2025, A&A, 696, A236
Perna, M., Arribas, S., Ji, X., et al. 2025, A&A, 694, A170
Péroux, C., & Howk, J. C. 2020, ARA&A, 58, 363
Peroux, C., & Nelson, D. 2024, ArXiv e-prints [arXiv:2411.07988]
Péroux, C., Storrie-Lombardi, L. J., McMahon, R. G., Irwin, M., & Hook, I. M. 2001, AJ, 121, 1799
Perrotta, S., Coil, A. L., Rupke, D. S. N., et al. 2024, ApJ, 975, 263
Pillepich, A., Reiprich, T. H., Porciani, C., Borm, K., & Merloni, A. 2018, MNRAS, 481, 613
Planck Collaboration VI. 2020, A&A, 641, A6
Polzin, A., Kravtsov, A. V., Semenov, V. A., & Gnedin, N. Y. 2024, Open J. Astrophys., 7, 114
Popesso, P., Concas, A., Morselli, L., et al. 2019, MNRAS, 483, 3213
Popesso, P., Concas, A., Morselli, L., et al. 2020, MNRAS, 496, 2531
Popesso, P., Concas, A., Cresci, G., et al. 2023, MNRAS, 519, 1526
Rao, S. M., & Turnshek, D. A. 2000, ApJS, 130, 1
Rasia, E., Tripodi, R., Borgani, S., et al. 2025, A&A, 702, A182
Reddy, N. A., Steidel, C. C., Pettini, M., et al. 2008, ApJS, 175, 48
Rodighiero, G., Cimatti, A., Gruppioni, C., et al. 2010, A&A, 518, L25
Rodighiero, G., Renzini, A., Daddi, E., et al. 2014, MNRAS, 443, 19
Romeo, A. B. 2020, MNRAS, 491, 4843
Romeo, A. B., Agertz, O., & Renaud, F. 2020, MNRAS, 499, 5656
Rosdahl, J., Katz, H., Blaizot, J., et al. 2018, MNRAS, 479, 994
Rowland, L. E., Heintz, K. E., Algera, H., et al. 2025, A&A, submitted [arXiv:2510.11351]
Rusta, E., Salvadori, S., Gelli, V., Koutsouridou, I., & Marconi, A. 2024, ApJ, 974, L35
Sabbi, E., Zeidler, P., Marel, R. P. v. d., et al. 2022, ApJ, 936, 135
Saintonge, A., Kauffmann, G., Kramer, C., et al. 2011, MNRAS, 415, 32
Saintonge, A., Catinella, B., Cortese, L., et al. 2016, MNRAS, 462, 1749
Saintonge, A., Catinella, B., Tacconi, L. J., et al. 2017, ApJS, 233, 22
Salak, D., Hashimoto, T., Inoue, A. K., et al. 2024, ApJ, 962, 1
Salpeter, E. E. 1955, ApJ, 121, 161
Salvestrini, F., Bianchi, S., & Corbelli, E. 2025, A&A, 699, A346
Santini, P., Fontana, A., Castellano, M., et al. 2017, ApJ, 847, 76
Santoro, F., & Shull, J. M. 2006, ApJ, 643, 26
Sargent, M. T., Daddi, E., Béthermin, M., et al. 2014, ApJ, 793, 19
Sarmento, R., & Scannapieco, E. 2025, ApJ, 988, 221
Saslaw, W. C., & Zipoy, D. 1967, Nature, 216, 976
Scarlata, C. M., Hu, W., Hayes, M. J., et al. 2025, ApJ, 985, 115
Schady, P., Yates, R. M., Christensen, L., et al. 2024, MNRAS, 529, 2807
Schouws, S., Bouwens, R. J., Algera, H., et al. 2025a, ApJ, submitted [arXiv:2502.01610]
Schouws, S., Bouwens, R. J., Ormerod, K., et al. 2025b, ApJ, 988, 19
Schreiber, C., Pannella, M., Elbaz, D., et al. 2015, A&A, 575, A74
Scoville, N., Sheth, K., Aussel, H., et al. 2016, ApJ, 820, 83
Shao, Y., Wang, R., Weiss, A., et al. 2022, A&A, 668, A121
Silk, J. 1983, MNRAS, 205, 705
Skinner, D., & Wise, J. H. 2020, MNRAS, 492, 4386
Speagle, J. S., Steinhardt, C. L., Capak, P. L., & Silverman, J. D. 2014, ApJS, 214, 15
Spilker, J. S., Champagne, J. B., Fan, X., et al. 2025, ApJ, 982, 72
Spina, B., Bosman, S. E. I., Davies, F. B., Gaikwad, P., & Zhu, Y. 2024, A&A, 688, L26
Spingola, C., McKean, J. P., Vegetti, S., et al. 2020, MNRAS, 495, 2387
Springel, V. 2005, MNRAS, 364, 1105
Stacy, A., McKee, C. F., Lee, A. T., Klein, R. I., & Li, P. S. 2022, MNRAS, 511, 5042
Stefanon, M., Bouwens, R. J., Labbé, I., et al. 2021, ApJ, 922, 29
Storrie-Lombardi, L. J., & Wolfe, A. M. 2000, ApJ, 543, 552
Szakacs, R., Péroux, C., Zwaan, M. A., et al. 2022, MNRAS, 512, 4736
Tacchella, S., Bose, S., Conroy, C., Eisenstein, D. J., & Johnson, B. D. 2018, ApJ, 868, 92
Tacconi, L. J., Neri, R., Genzel, R., et al. 2013, ApJ, 768, 74
Tacconi, L. J., Genzel, R., Saintonge, A., et al. 2018, ApJ, 853, 179
Tacconi, L. J., Genzel, R., & Sternberg, A. 2020, ARA&A, 58, 157
Tornatore, L., Ferrara, A., & Schneider, R. 2007, MNRAS, 382, 945
Tumlinson, J., Peeples, M. S., & Werk, J. K. 2017, ARA&A, 55, 389
Vanzella, E., Messa, M., Zanella, A., et al. 2026, A&A, 705, L12
Venditti, A., Graziani, L., Schneider, R., et al. 2023, MNRAS, 522, 3809
Viel, M., Haehnelt, M. G., Bolton, J. S., et al. 2017, MNRAS, 467, L86
Villaescusa-Navarro, F., Anglés-Alcázar, D., Genel, S., et al. 2021, ApJ, 915, 71
Vincenzo, F., Matteucci, F., Belfiore, F., & Maiolino, R. 2016, MNRAS, 455, 4183
Visbal, E., Bryan, G. L., & Haiman, Z. 2020, ApJ, 897, 95
Vizgan, D., Vieira, J. D., Spilker, J. S., et al. 2026, ApJ, in press [arXiv:2601.04133]
Walter, F., Carilli, C., Neeleman, M., et al. 2020, ApJ, 902, 111
Ward, S. R., Harrison, C. M., Costa, T., & Mainieri, V. 2022, MNRAS, 514, 2936
Weng, S., Sadler, E. M., Foster, C., et al. 2022, MNRAS, 512, 3638
Werk, J. K., Rubin, K. H. R., Bish, H. V., et al. 2019, ApJ, 887, 89
Whelan, J., & Iben, I., Jr 1973, ApJ, 186, 1007
Wise, J. H., Turk, M. J., Norman, M. L., & Abel, T. 2012, ApJ, 745, 50
Wolfe, A. M., Lanzetta, K. M., Foltz, C. B., & Chaffee, F. H. 1995, ApJ, 454, 698
Xu, H., Norman, M. L., O'Shea, B. W., & Wise, J. H. 2016, ApJ, 823, 140
Yoshida, N., Omukai, K., & Hernquist, L. 2007, ApJ, 667, L117
Zanchettin, M. V., Ramos Almeida, C., Audibert, A., et al. 2025, A&A, 695, A185
Zanella, A., Valentino, F., Gallazzi, A., et al. 2023, MNRAS, 524, 923
Zanella, A., Iani, E., Dessauges-Zavadsky, M., et al. 2024, A&A, 685, A80
Zanella, A., Belli, S., Valentino, F. M., & Bolamperti, A. 2026, A&A, in press https://doi.org/10.1051/0004-6361/202558073
Zang, S.-H., & Zhu, H.-M. 2024, ApJ, 961, 160
Zavala, J. A., Casey, C. M., Scoville, N., et al. 2019, ApJ, 887, 183
Zavala, J. A., Casey, C. M., Spilker, J., et al. 2022, ApJ, 933, 242
Zhang, Y., Comparat, J., Ponti, G., et al. 2024a, A&A, 690, A267
Zhang, Y., Comparat, J., Ponti, G., et al. 2024b, A&A, 690, A268
Zhu, H., Avestruz, C., & Gnedin, N. Y. 2020, ApJ, 899, 137
Zhu, Y., Becker, G. D., Bosman, S. E. I., et al. 2024, MNRAS, 533, L49

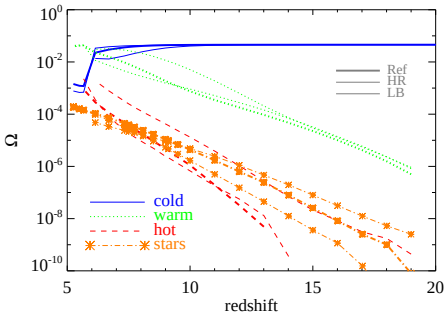



**Fig. A.1.** Redshift evolution of the mass density parameters for the cold (solid lines), warm (dotted lines), hot (dashed lines) and stellar (dot-dashed lines) components in the Ref (thick lines), HR (regular lines) and LB (thin lines) simulations.

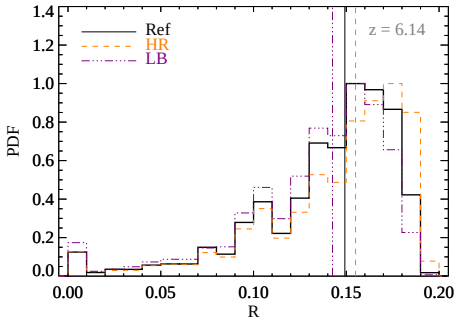



**Fig. A.2.** Probability distributions (histograms) and median values (vertical lines) of $R$ for the Ref (solid black lines), HR (dashed orange lines) and LB (dot-dot-dot-dashed purple lines) simulations at $z \simeq 6$.

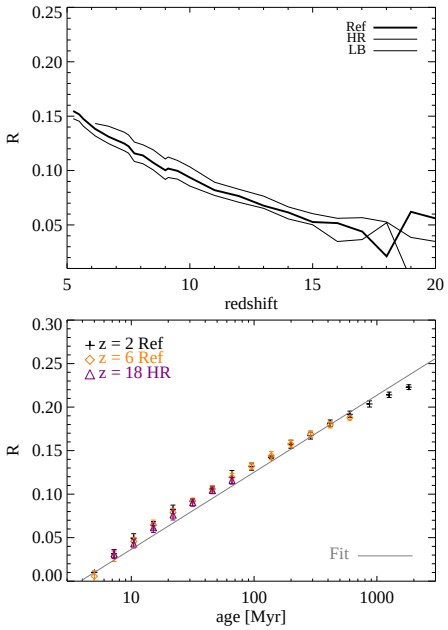



**Fig. A.3.** Top: Redshift evolution of the average $R$ at different redshifts for the Ref (solid black lines), HR (dashed orange lines) and LB (dot-dot-dot-dashed purple lines) simulations. Bottom: Dependence of $R$ on stellar age at $z \simeq 2$ (crosses), 6 (diamonds) and 18 (triangles), plotted together with the fitting function of eq. 2 (solid line).

## Appendix A: Numerical effects

In Fig. A.1 the impact of different box resolutions and sizes on the evolution of the matter density parameters is shown for cold, warm, hot and stellar phases in the Ref, HR, and LB runs. Results converge to the same behaviour in all the boxes.

Figs. A.2 and A.3 show the resulting distributions for the stellar return fraction $R$ at $z \simeq 6$, and its evolution as function of redshift and stellar age, as described by the fitting expression of eq. 2: $R(t_{\rm age}) = 0.0885\,{\rm Log}(t_{\rm age}/3.853{\rm Myr})$. $R$ values are obtained from self-consistent stellar-evolution calculations including time-dependent metal enrichment for a Salpeter IMF.

Further numerical effects are discussed about stellar-metallicity dependences of the stellar return fraction $R$ in Fig. A.4. We find metallicity-driven variations from a few up to some ten percent with stronger impacts at high redshift, as demonstrated by the $R$ distributions for metallicity-selected structures ($Z < 0.001\,{\rm Z}_\odot$ and $Z > 0.1\,{\rm Z}_\odot$). At $z \simeq 6$, 9 and 12, sample peak and median are both around $R \simeq 0.15$, 0.11 and 0.09. Metal-poor populations, that are older and more evolved, feature corresponding values of $R \sim 0.17$, 0.12 and 0.09, while younger metal-rich populations have $R \sim 0.14$, 0.09 and 0.06.

## Appendix B: Selection effects

In Fig. B.1, we show halo mass functions obtained with different selection criteria. Total-mass functions and virial-mass functions feature similar trends, with slight differences in the low-mass tail. When haloes with more than 300 member particles are considered, the low-mass tail is statistically less populated as tiny objects, presumably not well resolved, are excluded.

In Fig. B.2 we show the impacts of selection effects in terms of the relative contribution to the total mass locked in bound objects when different mass or number thresholds are applied.

## Appendix C: Main sequence

With the selection performed in this work (more than 300 particles to resolve the virial mass of haloes), we retrieve the basic relations involving SFR, stellar mass and halo mass at different epochs, as plotted in Fig. C.1. The simulated main sequence at different $z$ (upper panel) can be fitted by eq. 1 with the values of the parameters $a$ and $b$ listed in Table F.1. The values we find are in good agreement with $z \simeq 5$ observational determinations (Rodighiero et al. 2010, 2014; Kashino et al. 2013; Speagle et al. 2014; Schreiber et al. 2015; Popesso et al. 2023; Herrera-Camus et al. 2025). The simulated relation between stellar mass and halo mass (lower panel) features a generally increasing trend at all $z$. Recent literature works adopting heterogeneous numerical techniques are in line with the broad scatter we find at low masses (Ceverino et al. 2017; Rosdahl et al. 2018; Tacchella et al. 2018; Behroozi et al. 2019; Zhu et al. 2020; Romeo et al. 2020; Stefanon et al. 2021).

## Appendix D: Mass fractions and phases

In the top panel of Fig. D.1 the ratios between the bound-object mass density parameters and the cosmic mass density parameters are shown for each baryon phase. Similarly, results for the IGM-to-cosmic ratios are shown in the bottom panel. At early times, most of the cosmic gas is in the cold (HI) phase, but, due to the rarity of primordial objects, cold bound gas accounts for only $\Omega_{\rm bound,cold}/\Omega_{\rm cold} \lesssim 10^{-4}$ ($z \simeq 18$). The amount of warm cosmic gas is tiny in comparison to cold cosmic gas (Fig. 2) and is typically bound ($\Omega_{\rm bound,warm}/\Omega_{\rm warm} > 50\%$ at $z \simeq 18$). While cosmic evolution proceeds, more and more gas experiences cooling, star

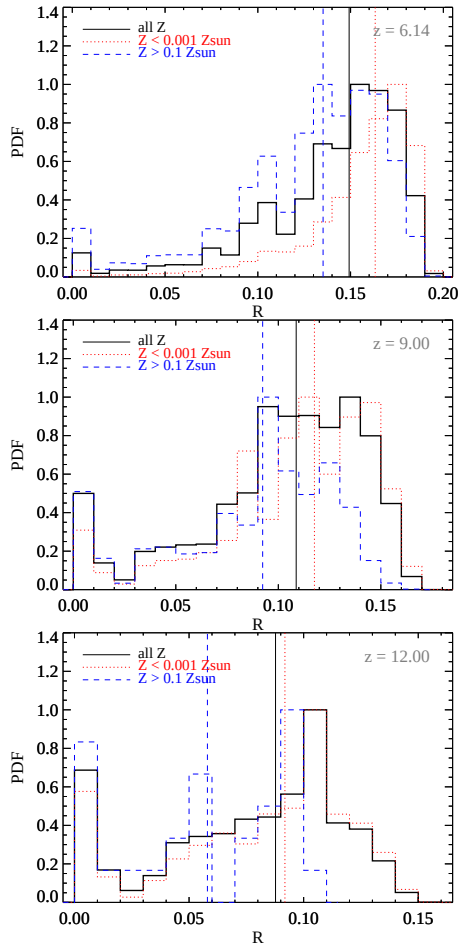



**Fig. A.4.** Probability distribution functions (histograms) and median values (vertical lines) of $R$ computed for the Ref run at redshift $z \simeq 6$, 9 and 12 for different stellar metallicities: all $Z$ (solid black lines), $Z < 0.001 Z_{\odot}$ (dotted red lines) and $Z > 0.1 Z_{\odot}$ (dashed blue lines).

formation and feedback effects in growing galaxies. These processes boost $\Omega_{\rm bound,H_2}/\Omega_{\rm H_2}$ up to ∼0.8, lower $\Omega_{\rm IGM,H_2}/\Omega_{\rm H_2}$ down to ∼0.2 and lead to $\Omega_{\rm bound,hot}/\Omega_{\rm hot} \sim 0.1$–1% at $z \simeq 6$–10.

In Fig. D.2, we display the mean redshift evolution of the bound-object mass fractions for the cold, warm, hot, stellar, HI and $H_2$ baryon phase, computed as $< f_{\rm phase} >= M_{\rm phase}/M_{\rm gas} = \Omega_{\rm bound,phase}/(\Omega_{\rm bound,cold} + \Omega_{\rm bound,warm} + \Omega_{\rm bound,hot})$, where, $M_{\rm phase}$ and $M_{\rm gas}$ are the total bound masses in the considered phase and in the gas, respectively. Clearly, the cold and warm phases dominate the halo mass content at $z \gtrsim 6$ and $z \lesssim 6$, respectively, and the cold and warm fractions lie around 0.3 and 0.7 at $z \simeq 5$. Hot gas is always subdominant, with average fractions that increase from $\sim 10^{-6}$ at $z \simeq 10$ to about $5 \times 10^{-3}$ at $z \simeq 5$, while star fractions follow star formation activity increasing from $\sim 10^{-4}$ at $z \simeq 19$ to 0.1 at $z \simeq 5$. HI and $H_2$ phases feature trends that are almost flat with average $H_2$-to-HI ratios ∼0.001-0.05.

Cold, warm and hot simulated gas fractions at different $z$ as functions of virial mass, stellar mass, SFR and gas $Z$ are displayed in Fig. D.3, while the trends for HI and $H_2$ gas fractions are presented in Fig. D.4. These quantities are theoretically consistent, but they are hard to be proven observationally, since detecting all the gaseous components and estimating the total gas mass in galaxies is challenging. So, in Fig. D.5, we normalise the HI and $H_2$ fractions by accounting for the cold component only, i.e.:

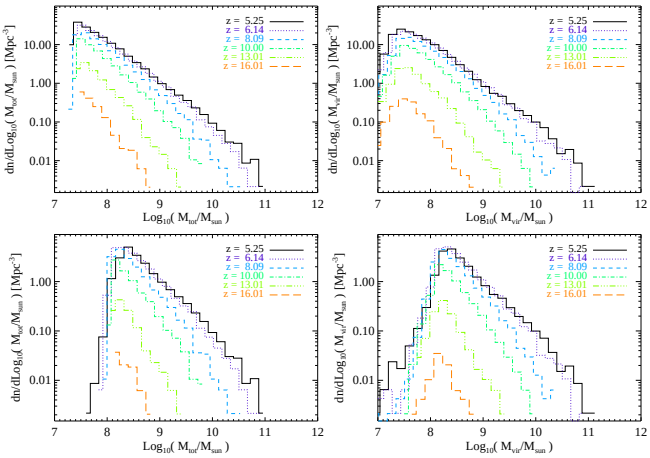



**Fig. B.1.** Top row: Halo total-mass functions (left) and virial-mass functions (right) at $z = 5.25$, 6.14, 8.09, 10.00, 13.01, 16.00. Bottom row: Corresponding functions for haloes with more than 300 particles.

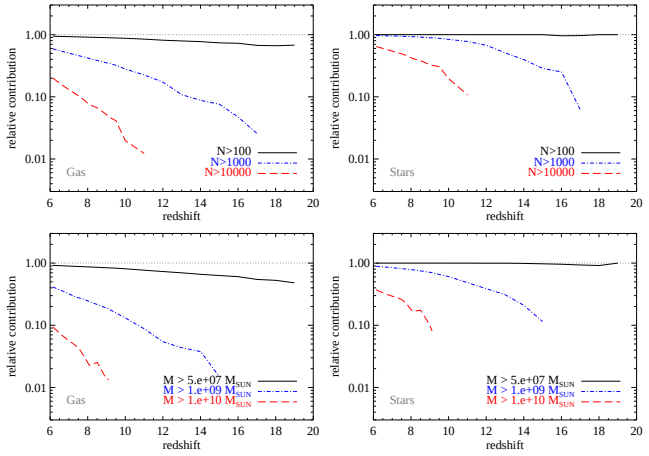



**Fig. B.2.** Top row: Contribution to the total gas mass (left) and stellar mass (right) of haloes with a number of particles $N > 100$ (solid lines), 1 000 (dot-dashed lines), 10 000 (dashed lines) as a function of redshift. Bottom row: Contribution of haloes with total mass $M > 5 \times 10^7$ (solid lines), $10^9$ (dot-dashed lines) and $10^{10}$ $M_{\odot}$ (dashed lines).

$f_{\rm HI,cold} = M_{\rm HI}/M_{\rm cold}$ and $f_{\rm H_2,cold} = M_{\rm H_2}/M_{\rm cold}$. These quantities are closer to observations when HI and/or $H_2$ can be considered good tracers of the gas budget (e.g. Bacchini et al. 2019, 2024). The figures show $f_{\rm HI,cold} \simeq 0.75$ for all the galaxy populations sampled at different $z$, while $f_{\rm H_2,cold}$ reaches values up to $\sim$ 0.2–0.3, i.e. some dex higher than $f_{\rm H_2}$. These results are consequences of the fact that HI is only present in the cold phase, where most $H_2$ is formed. In general, $H_2$ molecules are susceptible to non-equilibrium, environment and feedback effects, as highlighted by the scatter in both $f_{\rm H_2}$ (Fig. D.4) and $f_{\rm H_2,cold}$ (Fig. D.5). These results are consistent with Figs. 6 and 7.

## Appendix E: Depletion times

HI and $H_2$ gas depletion times as function of stellar mass $M_{\rm star}$, gas metallicity $Z$ and sSFR can be found in Fig. E.1. Data points show rather broad relations due to the role of feedback and environment in shaping gas properties at all times. The values of $t_{\rm depl,HI}$ and $t_{\rm depl,H_2}$ decrease with stellar mass and metallicity and minimum values are reached in star-forming structures with $M_{\rm star} \sim 10^8$–$10^9$ $M_{\odot}$ and $Z > 0.01\, Z_{\odot}$. The similarity of these

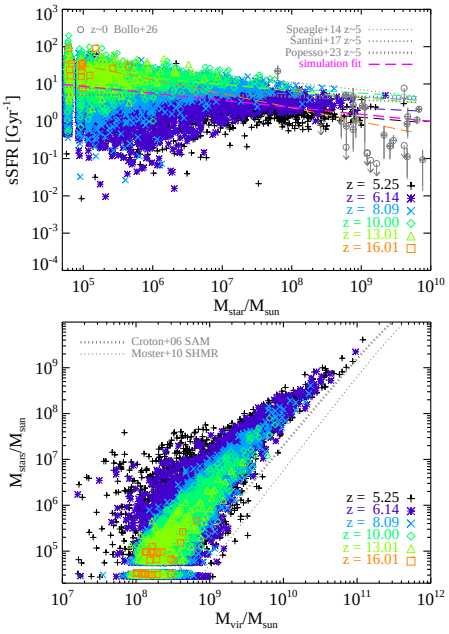



**Fig. C.1.** Top: Simulated sSFR and $M_{\rm star}$ at different $z$ (coloured symbols), $z \simeq 5$ observational fits by Speagle et al. (2014), Santini et al. (2017) and Popesso et al. (2023) (thin, regular and thick dotted lines) and $z \sim 0.5$ MUSE-ALMA determinations (circles) with upper limits (arrows) by Bollo et al. (2026). Fits to simulation data at each $z$ (thin dashed lines) are displayed together with the fit to the whole simulated sample (thick dashed magenta line), as per eq. 1 and Table F.1: $\mathrm{Log_{10}(sSFR/Gyr^{-1})} = 1.871 - 0.187\,\mathrm{Log_{10}(M_{star}/M_\odot)}$. Bottom: Simulated $M_{\rm star}$ and $M_{\rm vir}$ and fits from a low-$z$ semi-analytical model (Croton et al. 2006, SAM, thick dotted line) and the stellar-to-halo mass relation (Moster et al. 2010, SHMR, thin dotted line).

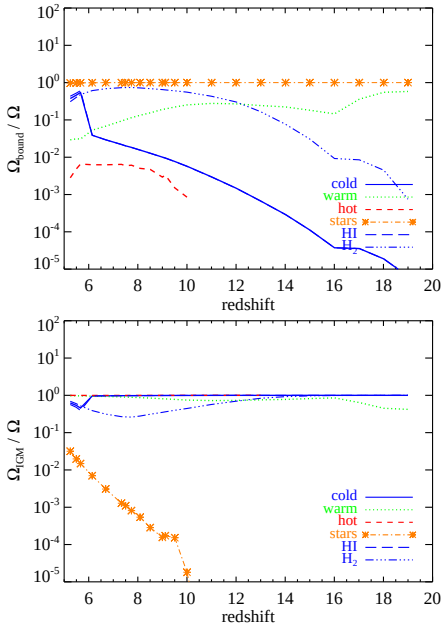



**Fig. D.1.** Bound-to-cosmic (top) and IGM-to-cosmic (bottom) mass density ratio for the cold, warm, hot, stellar, HI and $H_2$ baryon phases.

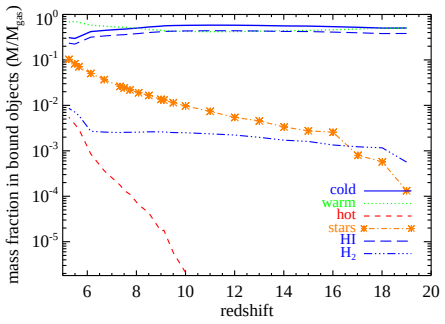



**Fig. D.2.** Average mass fraction of each baryon phase (cold, warm, hot, stars, HI, $H_2$) identified in bound objects at different redshifts.

trends with the ones with SFR in Fig. 10 is simply understood in terms of the main-sequence and mass-metallicity relations.

## Appendix F: Fitting functions

We fit simulated results in the base-10 logarithmic form

$$\mathrm{Log}\, y = a + b\,\mathrm{Log}\, x$$

where $x$ and $y$ are dimensionless, non-negative variables and $a$ and $b$ are fit parameters.

We consider data for masses, SFR and metallicities both at individual redshifts and in the whole $z > 5$ range (all $z$). Masses and metallicities are expressed in solar units, SFR in $\mathrm{M_\odot yr^{-1}}$, depletion times in Gyr and sSFR in $\mathrm{Gyr^{-1}}$.

In Table F.1 we report $a$ and $b$ parameters for the main sequence and the relations between $M_{\rm cold}$, $M_{\rm warm}$, $M_{\rm hot}$ vs $M_{\rm star}$ or SFR:

$\mathrm{Log(sSFR/Gyr^{-1})} = a + b\,\mathrm{Log}(M_{\rm star}/\mathrm{M_\odot})$
$\mathrm{Log}(M_{\rm cold}/\mathrm{M_\odot}) = a + b\,\mathrm{Log}(M_{\rm star}/\mathrm{M_\odot})$
$\mathrm{Log}(M_{\rm warm}/\mathrm{M_\odot}) = a + b\,\mathrm{Log}(M_{\rm star}/\mathrm{M_\odot})$
$\mathrm{Log}(M_{\rm hot}/\mathrm{M_\odot}) = a + b\,\mathrm{Log}(M_{\rm star}/\mathrm{M_\odot})$
$\mathrm{Log}(M_{\rm cold}/\mathrm{M_\odot}) = a + b\,\mathrm{Log[SFR/(M_\odot\,yr^{-1})]}$
$\mathrm{Log}(M_{\rm warm}/\mathrm{M_\odot}) = a + b\,\mathrm{Log[SFR/(M_\odot\,yr^{-1})]}$
$\mathrm{Log}(M_{\rm hot}/\mathrm{M_\odot}) = a + b\,\mathrm{Log[SFR/(M_\odot\,yr^{-1})]}$.

Parameter determinations for the $M_{\rm hot}$ relations are missing at $z \gtrsim 10$ due to lack of statistics. To remove resolution artefacts, we fit the data for objects with stellar masses and hot-gas masses above $2 \times 10^6\,\mathrm{M_\odot}$ and SFR$> 3 \times 10^{-2}\,\mathrm{M_\odot\,yr^{-1}}$.

In Table F.2 we quote $a$ and $b$ parameters for the relations between $M_{\rm HI}$ or $\mathrm{M_{H_2}}$ and $M_{\rm vir}$ or $M_{\rm star}$ and for the relations between $M_{\rm HI}$ or $\mathrm{M_{H_2}}$ and SFR:

$\mathrm{Log}(M_{\rm HI}/\mathrm{M_\odot}) = a + b\,\mathrm{Log}(M_{\rm vir}/\mathrm{M_\odot})$
$\mathrm{Log}(M_{\rm H_2}/\mathrm{M_\odot}) = a + b\,\mathrm{Log}(M_{\rm vir}/\mathrm{M_\odot})$
$\mathrm{Log}(M_{\rm HI}/\mathrm{M_\odot}) = a + b\,\mathrm{Log}(M_{\rm star}/\mathrm{M_\odot})$
$\mathrm{Log}(M_{\rm H_2}/\mathrm{M_\odot}) = a + b\,\mathrm{Log}(M_{\rm star}/\mathrm{M_\odot})$
$\mathrm{Log}(M_{\rm HI}/\mathrm{M_\odot}) = a + b\,\mathrm{Log[SFR/(M_\odot\,yr^{-1})]}$
$\mathrm{Log}(M_{\rm H_2}/\mathrm{M_\odot}) = a + b\,\mathrm{Log[SFR/(M_\odot\,yr^{-1})]}$.

Results for HI and $H_2$ gas-to-star fractions $\mu_{\rm HI} = M_{\rm HI}/M_{\rm star}$ and $\mu_{\rm H_2} = M_{\rm H_2}/M_{\rm star}$ as functions of $M_{\rm star}$ are also fitted as:

$\mathrm{Log}\mu_{\rm HI} = a + b\,\mathrm{Log}(M_{\rm star}/\mathrm{M_\odot})$
$\mathrm{Log}\mu_{\rm H_2} = a + b\,\mathrm{Log}(M_{\rm star}/\mathrm{M_\odot})$.

Corresponding $F_{\rm gas}$ values are obtained via $F_{\rm gas} = \mu_{\rm H_2}/(\mu_{\rm H_2} + 1)$.

Fit parameters for HI and $H_2$ depletion times, $t_{\rm depl,HI}$ and $t_{\rm depl,H_2}$, as functions of $M_{\rm star}$, SFR, gas $Z$ and sSFR are quoted in Table F.3 for the expressions below:

$\mathrm{Log}(t_{\rm depl,HI}/\mathrm{Gyr}) = a + b\,\mathrm{Log}(M_{\rm star}/\mathrm{M_\odot})$
$\mathrm{Log}(t_{\rm depl,H_2}/\mathrm{Gyr}) = a + b\,\mathrm{Log}(M_{\rm star}/\mathrm{M_\odot})$
$\mathrm{Log}(t_{\rm depl,HI}/\mathrm{Gyr}) = a + b\,\mathrm{Log[SFR/(M_\odot\,yr^{-1})]}$
$\mathrm{Log}(t_{\rm depl,H_2}/\mathrm{Gyr}) = a + b\,\mathrm{Log[SFR/(M_\odot\,yr^{-1})]}$
$\mathrm{Log}(t_{\rm depl,HI}/\mathrm{Gyr}) = a + b\,\mathrm{Log}(Z/Z_\odot)$
$\mathrm{Log}(t_{\rm depl,H_2}/\mathrm{Gyr}) = a + b\,\mathrm{Log}(Z/Z_\odot)$
$\mathrm{Log}(t_{\rm depl,HI}/\mathrm{Gyr}) = a + b\,\mathrm{Log(sSFR/Gyr^{-1})}$

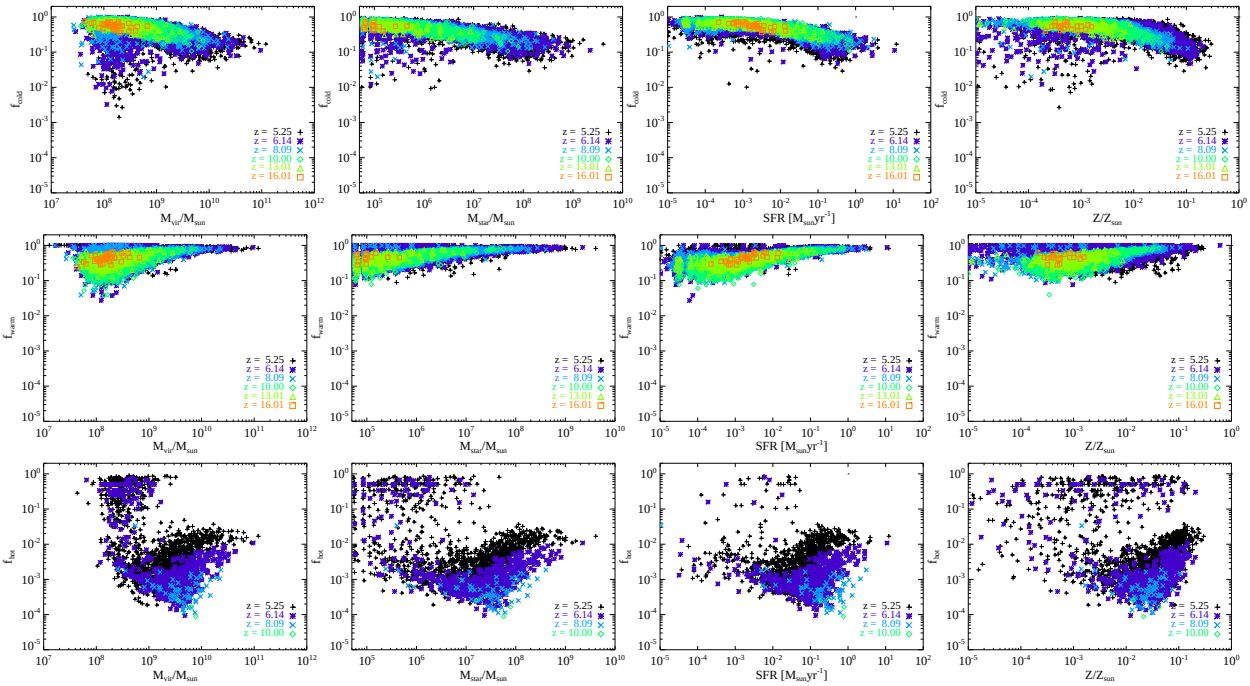


**Fig. D.3.** Cold (top row), warm (central row) and hot (bottom row) gas fraction versus virial mass (first column), stellar mass (second column), SFR (third column) and gas metallicity (fourth column) at $z$ =5.25, 6.14, 8.09, 10.00, 13.01, and 16.01.

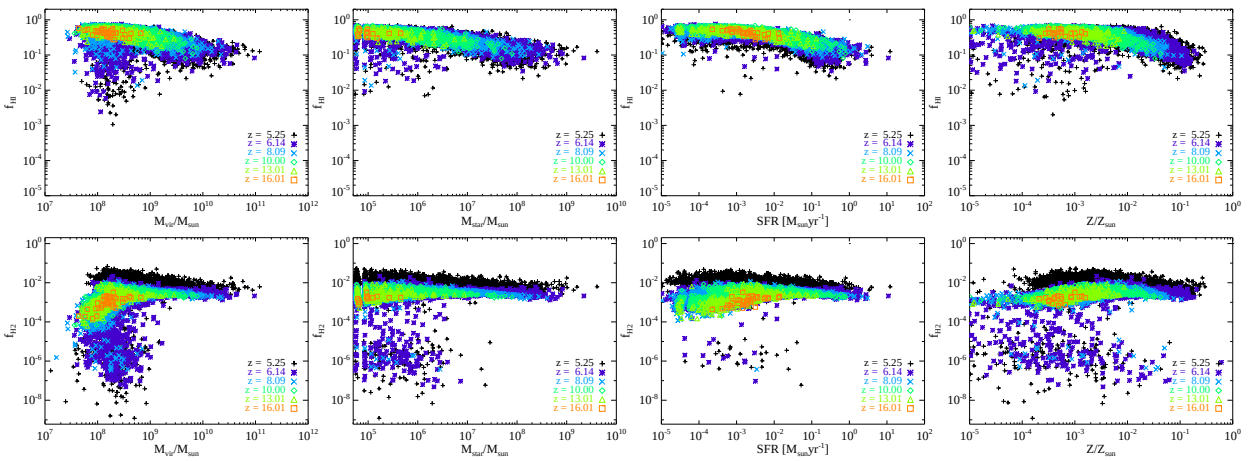


**Fig. D.4.** HI (top) and $H_2$ (bottom) mass fractions versus virial mass, stellar mass, SFR and gas metallicity, respectively from left to right, at $z$ =5.25, 6.14, 8.09, 10.00, 13.01, and 16.01.

$\mathrm{Log}(t_{\mathrm{depl,H_2}}/\mathrm{Gyr}) = a + b\,\mathrm{Log}(\mathrm{sSFR}/\mathrm{Gyr}^{-1})$.

Redshift evolution of the median $t_{\mathrm{depl,HI}}$ and $t_{\mathrm{depl,H_2}}$ is:
$\mathrm{Log}(t_{\mathrm{depl,HI}}/\mathrm{Gyr}) = 1.345 - 0.170\,\mathrm{Log}(1+z)$
$\mathrm{Log}(t_{\mathrm{depl,H_2}}/\mathrm{Gyr}) = 0.943 - 2.045\,\mathrm{Log}(1+z)$.
Their behaviour is bracketed by the average trends
$\mathrm{Log}(t_{\mathrm{depl,HI}}/\mathrm{Gyr}) = -1.177 + 1.578\,\mathrm{Log}(1+z)$
$\mathrm{Log}(t_{\mathrm{depl,H_2}}/\mathrm{Gyr}) = -1.499 - 0.236\,\mathrm{Log}(1+z)$
and the mean trends
$\mathrm{Log}(t_{\mathrm{depl,HI}}/\mathrm{Gyr}) = 2.857 - 1.301\,\mathrm{Log}(1+z)$
$\mathrm{Log}(t_{\mathrm{depl,H_2}}/\mathrm{Gyr}) = 2.273 - 3.065\,\mathrm{Log}(1+z)$.
The evolution of the average $\mu_{\mathrm{HI}}$ and $\mu_{\mathrm{H_2}}$ is given by:
$\mathrm{Log}\,\mu_{\mathrm{HI}} = -3.379 + 4.813\,\mathrm{Log}(1+z)$
$\mathrm{Log}\,\mu_{\mathrm{H_2}} = -3.700 + 2.300\,\mathrm{Log}(1+z)$
with $F_{\mathrm{gas}} = \mu_{\mathrm{H_2}}/(\mu_{\mathrm{H_2}}+1)$.

We fit the recovery timescale for 15-200 $\mathrm{M}_\odot$ stars as:
$\mathrm{Log}(t_{\mathrm{rec}}/\mathrm{Myr}) = 3.295 - 2.349\mathrm{Log}(t_{\mathrm{age}}/\mathrm{Myr})$, equivalent to
$\mathrm{Log}(t_{\mathrm{rec}}/\mathrm{Myr}) = -0.424 + 1.307\mathrm{Log}(M_{\mathrm{star}}/\mathrm{M}_\odot)$.

The fitting function for the stellar return fraction $R$ (eq. 2) is:

$$R(t_{\mathrm{age}}) = 0.0885\,\mathrm{Log}\left(\frac{t_{\mathrm{age}}}{3.853\,\mathrm{Myr}}\right)$$

for stellar ages $t_{\mathrm{age}} > 3.853$ Myr and $R = 0$ otherwise.

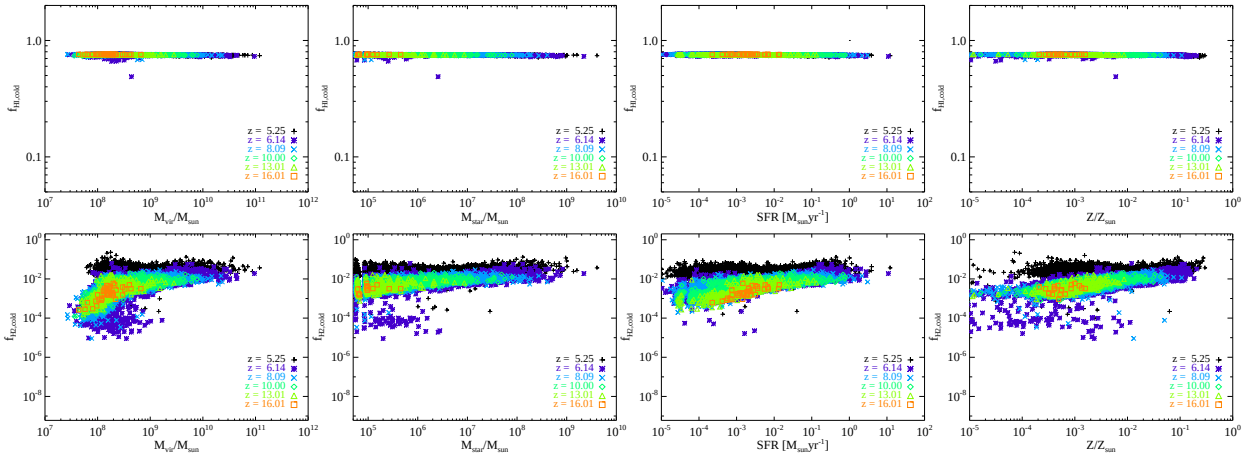


**Fig. D.5.** HI (top) and $H_2$ (bottom) cold-mass fractions versus virial mass, stellar mass, SFR and gas metallicity, respectively from left to right, at $z$ =5.25, 6.14, 8.09, 10.00, 13.01, and 16.01.

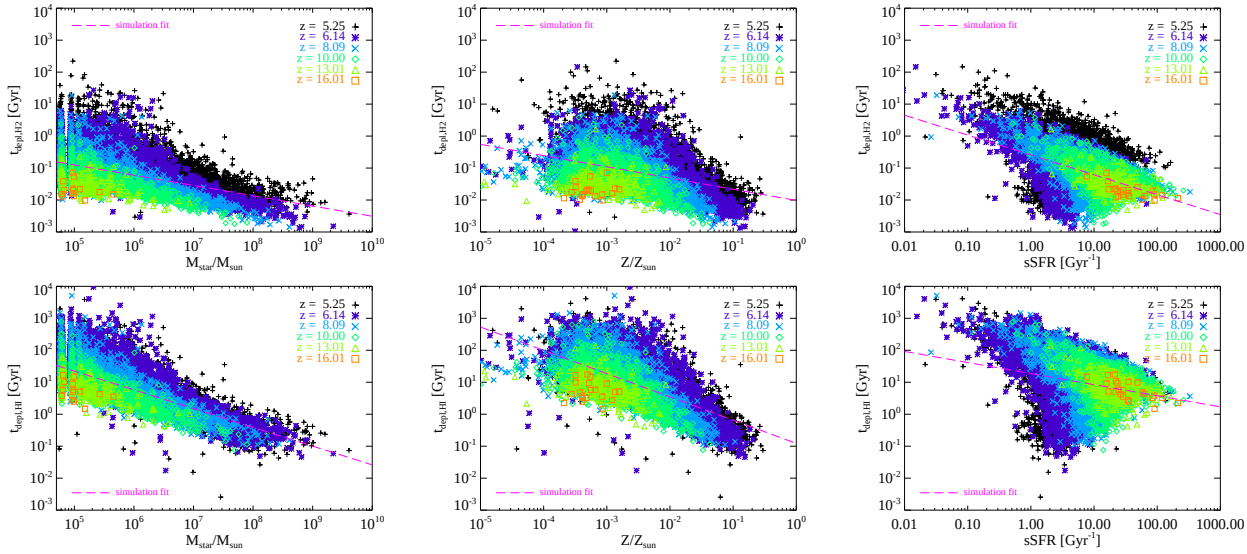


**Fig. E.1.** $H_2$ (top) and HI (bottom) depletion times versus stellar mass (left), gas metallicity (centre) and sSFR (right) at $z$ =5.25, 6.14, 8.09, 10.00, 13.01, and 16.01. Simulation fits (dashed magenta lines) are in Appendix F.

**Table F.1.** Fit parameters for the main sequence (sSFR vs. $M_{\rm star}$) and the relations between $M_{\rm cold}$ or $M_{\rm warm}$ or $M_{\rm hot}$ and $M_{\rm star}$ or SFR. Mass is in solar units, SFR in solar masses per year and sSFR in $\rm Gyr^{-1}$.

| $z$ | sSFR-$M_{\rm star}$ | | $M_{\rm cold}$-$M_{\rm star}$ | | $M_{\rm warm}$-$M_{\rm star}$ | | $M_{\rm hot}$-$M_{\rm star}$ | | $M_{\rm cold}$-SFR | | $M_{\rm warm}$-SFR | | $M_{\rm hot}$-SFR | |
|---|---|---|---|---|---|---|---|---|---|---|---|---|---|---|
| | $a$ | $b$ | $a$ | $b$ | $a$ | $b$ | $a$ | $b$ | $a$ | $b$ | $a$ | $b$ | $a$ | $b$ |
| all | 1.871 | -0.187 | 6.199 | 0.237 | 4.615 | 0.495 | 1.602 | 0.645 | 8.156 | 0.239 | 8.715 | 0.492 | 7.139 | 0.625 |
| 16.01 | 3.370 | -0.376 | 5.275 | 0.407 | 4.891 | 0.469 | - | - | 7.942 | 0.271 | 8.741 | 0.601 | - | - |
| 13.01 | 2.212 | -0.175 | 6.029 | 0.262 | 4.512 | 0.526 | - | - | 8.021 | 0.257 | 8.440 | 0.480 | - | - |
| 10.00 | 1.787 | -0.115 | 6.153 | 0.254 | 4.179 | 0.581 | - | - | 8.111 | 0.242 | 8.598 | 0.531 | - | - |
| 8.09 | 1.464 | -0.091 | 6.031 | 0.274 | 4.499 | 0.529 | -2.716 | 1.090 | 8.178 | 0.252 | 8.615 | 0.474 | 6.369 | 0.484 |
| 6.14 | 1.185 | -0.093 | 6.109 | 0.254 | 4.646 | 0.491 | -0.366 | 0.852 | 8.193 | 0.230 | 8.746 | 0.463 | 6.853 | 0.849 |
| 5.25 | 1.531 | -0.158 | 6.185 | 0.228 | 4.380 | 0.517 | 1.033 | 0.723 | 8.130 | 0.234 | 8.818 | 0.487 | 7.398 | 0.905 |

**Table F.2.** Fit parameters for $M_{\rm HI}$ or $\rm M_{H_2}$ and $M_{\rm vir}$, $M_{\rm star}$ and SFR relations, as well as for gas-to-star fractions $\mu_{\rm HI}$ and $\mu_{\rm H_2}$ versus $M_{\rm star}$ with mass in solar units and SFR in solar masses per year.

| $z$ | $M_{\rm HI}$-$M_{\rm vir}$ | | $M_{\rm H_2}$-$M_{\rm vir}$ | | $M_{\rm HI}$-$M_{\rm star}$ | | $M_{\rm H_2}$-$M_{\rm star}$ | | $M_{\rm HI}$-SFR | | $M_{\rm H_2}$-SFR | | $\mu_{\rm HI}$-$M_{\rm star}$ | | $\mu_{\rm H_2}$-$M_{\rm star}$ | |
|---|---|---|---|---|---|---|---|---|---|---|---|---|---|---|---|---|
| | $a$ | $b$ | $a$ | $b$ | $a$ | $b$ | $a$ | $b$ | $a$ | $b$ | $a$ | $b$ | $a$ | $b$ | $a$ | $b$ |
| all | 1.710 | 0.659 | -2.577 | 0.926 | 6.084 | 0.236 | 2.156 | 0.505 | 8.031 | 0.238 | 6.496 | 0.484 | 6.084 | -0.764 | 2.443 | -0.489 |
| 16.01 | -0.029 | 0.862 | -4.530 | 1.115 | 5.160 | 0.406 | 1.240 | 0.708 | 7.820 | 0.271 | 6.625 | 0.773 | 5.160 | -0.594 | 1.240 | -0.293 |
| 13.01 | 0.303 | 0.828 | -3.041 | 0.956 | 5.916 | 0.261 | 2.038 | 0.561 | 7.896 | 0.256 | 6.517 | 0.647 | 5.916 | -0.739 | 2.038 | -0.439 |
| 10.00 | 1.126 | 0.737 | -3.619 | 1.030 | 6.035 | 0.253 | 2.455 | 0.501 | 7.986 | 0.241 | 6.392 | 0.519 | 6.035 | -0.747 | 2.455 | -0.499 |
| 8.09 | 0.911 | 0.759 | -3.546 | 1.024 | 5.916 | 0.273 | 2.143 | 0.549 | 8.054 | 0.251 | 6.478 | 0.526 | 5.916 | -0.727 | 2.157 | -0.451 |
| 6.14 | 1.300 | 0.707 | -2.881 | 0.945 | 5.993 | 0.253 | 1.862 | 0.534 | 8.068 | 0.229 | 6.451 | 0.476 | 5.993 | -0.747 | 2.249 | -0.481 |
| 5.25 | 2.106 | 0.603 | 0.923 | 0.577 | 6.073 | 0.226 | 1.053 | 0.652 | 8.004 | 0.233 | 6.506 | 0.298 | 6.073 | -0.774 | 3.899 | -0.671 |

**Table F.3.** Fit parameters for HI and $H_2$ depletion times $t_{\rm depl,HI}$ and $t_{\rm depl,H_2}$ in Gyr versus $M_{\rm star}$, SFR, gas $Z$ and sSFR with mass in solar units, SFR in solar masses per year, $Z$ in units of $Z_\odot$ and sSFR in $\rm Gyr^{-1}$.

| $z$ | $t_{\rm depl,HI}$-$M_{\rm star}$ | | $t_{\rm depl,H_2}$-$M_{\rm star}$ | | $t_{\rm depl,HI}$-SFR | | $t_{\rm depl,H_2}$-SFR | | $t_{\rm depl,HI}$-$Z$ | | $t_{\rm depl,H_2}$-$Z$ | | $t_{\rm depl,HI}$-sSFR | | $t_{\rm depl,H_2}$-sSFR | |
|---|---|---|---|---|---|---|---|---|---|---|---|---|---|---|---|---|
| | $a$ | $b$ | $a$ | $b$ | $a$ | $b$ | $a$ | $b$ | $a$ | $b$ | $a$ | $b$ | $a$ | $b$ | $a$ | $b$ |
| all | 4.283 | -0.587 | 0.704 | -0.321 | -0.969 | -0.761 | -2.443 | -0.508 | -0.913 | -0.728 | -2.013 | -0.350 | 1.270 | -0.347 | -0.591 | -0.621 |
| 16.01 | 1.790 | -0.218 | -2.131 | 0.083 | -1.180 | -0.729 | -2.375 | -0.227 | 0.388 | -0.100 | -1.168 | 0.168 | 1.679 | -0.605 | -1.071 | -0.423 |
| 13.01 | 3.704 | -0.564 | -0.174 | -0.264 | -1.104 | -0.744 | -2.483 | -0.353 | -0.386 | -0.393 | -1.724 | -0.070 | 1.466 | -0.468 | -0.946 | -0.426 |
| 10.00 | 4.251 | -0.632 | 0.672 | -0.385 | -1.014 | -0.759 | -2.608 | -0.481 | -1.146 | -0.714 | -2.444 | -0.379 | 1.506 | -0.473 | -0.734 | -0.510 |
| 8.09 | 4.472 | -0.638 | 0.731 | -0.366 | -0.946 | -0.749 | -2.519 | -0.473 | -1.195 | -0.799 | -2.405 | -0.420 | 1.600 | -0.586 | -0.603 | -0.656 |
| 6.14 | 4.962 | -0.676 | 1.318 | -0.425 | -0.932 | -0.771 | -2.516 | -0.527 | -1.038 | -0.840 | -2.375 | -0.497 | 1.444 | -0.575 | -0.681 | -0.688 |
| 5.25 | 4.617 | -0.626 | 2.749 | -0.565 | -0.996 | -0.767 | -2.350 | -0.706 | -1.071 | -0.840 | -2.357 | -0.746 | 0.955 | -0.209 | -0.522 | -0.244 |